

Gradient Structure Estimation under Label-Only Oracles via Spectral Sensitivity

Jun Liu

State Key Laboratory of Internet of Things for Smart City, University of Macau; National Institute of Informatics, Tokyo, Japan
cjunliu@nii.ac.jp

Leo Yu Zhang

Griffith University
Gold Coast, Australia
leo.zhang@griffith.edu.au

Fengpeng Li

State Key Laboratory of Internet of Things for Smart City, University of Macau, China
yc17420@connect.um.edu.mo

Isao Echizen

The University of Tokyo; National Institute of Informatics
Tokyo, Japan
iechizen@nii.ac.jp

Jiantao Zhou

State Key Laboratory of Internet of Things for Smart City, University of Macau, China
jtzhou@umac.mo

Abstract

Hard-label black-box settings, where only top-1 predicted labels are observable, pose a fundamentally constrained yet practically important feedback model for understanding model behavior. A central challenge in this regime is whether meaningful gradient information can be recovered from such discrete responses. In this work, we develop a unified theoretical perspective showing that a wide range of existing sign-flipping hard-label attacks can be interpreted as implicitly approximating the sign of the true loss gradient. This observation reframes hard-label attacks from heuristic search procedures into instances of gradient sign recovery under extremely limited feedback. Motivated by this first-principles understanding, we propose a new attack framework that combines a zero-query frequency-domain initialization with a Pattern-Driven Optimization (PDO) strategy. We establish theoretical guarantees demonstrating that, under mild assumptions, our initialization achieves higher expected cosine similarity to the true gradient sign compared to random baselines, while the proposed PDO procedure attains substantially lower query complexity than existing structured search approaches. We empirically validate our framework through extensive experiments on CIFAR-10, ImageNet, and ObjectNet, covering standard and adversarially trained models, commercial APIs, and CLIP-based models. The results show that our method consistently surpasses state-of-the-art hard-label attacks in both attack success rate and query efficiency, particularly in low-query regimes. Beyond image classification, our approach generalizes effectively to corrupted data (ImageNet-C), biomedical datasets (PathMNIST), and dense

prediction tasks such as semantic segmentation. Notably, it also successfully circumvents Blacklight, a state-of-the-art stateful defense, resulting in a 0% detection rate. Our code will be released publicly soon¹.

Keywords

Adversarial examples; Black-box attacks; Deep learning robustness;

ACM Reference Format:

Jun Liu, Leo Yu Zhang, Fengpeng Li, Isao Echizen, and Jiantao Zhou. 2026. Gradient Structure Estimation under Label-Only Oracles via Spectral Sensitivity. In . ACM, New York, NY, USA, 29 pages. <https://doi.org/10.1145/nnnnnnnnnnnnnnnn>

1 Introduction

Deep Neural Networks (DNNs) have been widely applied in real-world applications such as image classification [4, 23], speech recognition [64], face recognition [17, 32], and etc. However, previous researches [21, 35, 36, 57] reveal that DNNs can fail catastrophically when processing Adversarial Examples (AEs)—carefully crafted inputs that deceive DNNs while appearing benign to human observers. In image classification tasks, adversarial attacks for generating AEs can be categorized based on the adversary’s knowledge of the victim model. Broadly, they fall into three classes: white-box [14, 18, 63], gray-box [25], and black-box attacks [2, 6, 55]. In white-box attacks, the adversary has complete access to the victim model’s architecture and parameters, while gray-box attacks assume partial access. In contrast, black-box attacks assume no knowledge of either the architecture or internal parameters of the victim model and can be further classified by the type of output they leverage: soft-label (namely score-based) attacks [1, 24] exploiting classification confidence scores (e.g., softmax outputs) and hard-label (a.k.a. decision-based) attacks [8, 52, 54] relying solely on the top-1 predicted labels.

Among these attacks, hard-label attacks represent the most challenging and practical scenario [8, 10, 11, 54, 55]. Real-world

Permission to make digital or hard copies of all or part of this work for personal or classroom use is granted without fee provided that copies are not made or distributed for profit or commercial advantage and that copies bear this notice and the full citation on the first page. Copyrights for components of this work owned by others than the author(s) must be honored. Abstracting with credit is permitted. To copy otherwise, or republish, to post on servers or to redistribute to lists, requires prior specific permission and/or a fee. Request permissions from permissions@acm.org.

Conference’17, Washington, DC, USA

© 2026 Copyright held by the owner/author(s). Publication rights licensed to ACM.

ACM ISBN 978-x-xxxx-xxxx-x/YYYY/MM

<https://doi.org/10.1145/nnnnnnnnnnnnnnnn>

¹<https://github.com/csjunjun/DPAttack.git>

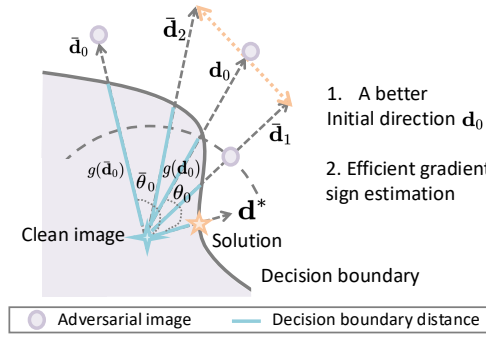


Figure 1: Comparison of our approach with traditional methods. Our method achieves a better initialization d_0 with smaller angular deviation θ_0 and boundary distance $g(d_0)$ compared to the traditional initialization d_0 . Furthermore, it employs a more query-efficient strategy to approximate the ideal descent direction d^* .

applications—such as industry AI systems (e.g., in medical imaging [15]) and commercial APIs (e.g., Core ML [3])—intentionally suppress output confidences due to data privacy regulations and mobile resource constraints, thereby necessitating decision-only attack strategies and making them crucial for evaluating and improving the robustness of DNNs. Hence, this paper primarily focuses on hard-label attacks.

Traditional hard-label attack workflow. Current hard-label attacks are broadly divided into surrogate-assisted and surrogate-free methods. Surrogate-assisted methods (or transfer-query attacks) leverage gradient priors from local models to guide the search [48]. Although efficient, their performance degrades significantly under architectural mismatch (e.g., Convolution Neural Networks (CNNs) vs. Transformers) or domain shifts, and can be mitigated by ensemble training [50]. In contrast, surrogate-free (query-based) methods operate independently of external priors, relying solely on the victim model’s hard-label feedback to estimate gradients or refine perturbations. The workflow of these query-based methods typically involves two stages:

Stage 1: Perturbation direction initialization. This stage aims to generate an initial search direction. Traditional methods randomly sample noise or another image until an AE is found. The vector from the clean image to this AE defines the initial direction. Then, a binary search is performed along this vector to locate a *starting point* close to the decision boundary.

Stage 2: Direction refinement and perturbation reduction. Starting from the boundary point, this stage iteratively refines the initial direction and reduces the perturbation magnitude based on hard-label feedback. The objective is to identify an AE that satisfies the specified perturbation constraints. If no valid example is found within the allocated query budget, the attack is deemed unsuccessful.

Observations and insights. **1) Better initialization.** We observe that most existing black-box attacks devote substantial effort to Stage 2 (the search phase), while largely overlooking the importance of Stage 1 (initialization). In practice, they typically rely on random strategies, such as Gaussian or Uniform noise [8, 12, 41, 54],

random images [39, 54], or all 1 perturbations [7, 55]. These choices ignore prior knowledge about model vulnerabilities, often producing initial directions that are far from the decision boundary and difficult to refine under limited query budgets (e.g., < 100 queries). This motivates us to design a prior-guided initialization that yields a superior starting direction d_0 . As illustrated in Fig. 1, our goal is to obtain an initialization that is closer to the ideal descent direction d^* , both in angular deviation and in decision-boundary distance, compared to conventional random starts.

2) More efficient gradient sign estimation. The next challenge is to efficiently approach the ideal descent direction d^* . Prior work such as SignHunter [1] shows that, with sufficient queries, it can approximate the gradient sign used in FGSM [28]. Similarly, we observe that RayS [7] can asymptotically achieve FGSM-level performance by iteratively refining sign estimates through sign-flipping. However, in practice, the efficiency of such methods deteriorates rapidly as the dimensionality grows. Moreover, when refining our structured initial directions, RayS-style rigid equal partitioning ignores the underlying spatial pattern, frequently breaking coherent regions into fragmented pieces. This leads to *gain cancellation*: when a partition contains conflicting gradient signs, their contributions offset one another, thereby weakening the effective descent signal and slowing the search process. These observations suggest that efficient gradient sign approximation requires not only reducing the search dimensionality, but also preserving spatial coherence throughout the search process.

Our work. From a *greedy optimization* perspective, we propose an efficient black-box attack that jointly improves initialization and search. First, we design a superior initialization strategy via Block-wise Discrete Cosine Transform (BDCT) analysis [53]. By characterizing model sensitivity across frequency bands, we derive a data-driven sampling distribution from the clean image’s frequency statistics and generate an initial direction via inverse BDCT. Both theoretical analysis and empirical results show that this initialization is significantly closer to the decision boundary and exhibits higher cosine similarity with the true gradient sign than random baselines (Sec. 4.3).

Building upon this structured initialization, we further introduce a *Pattern-Driven Optimization* (PDO) module. PDO explicitly preserves the spatial coherence of initial directions throughout the search process, thereby reducing the effective search dimensionality and mitigating gain cancellation. As a result, it approximates the ideal descent direction with substantially fewer queries than the equal partitioning searches used in state-of-the-art (SOTA) baselines (Sec. 4.4).

We summarize our main contributions as follows:

- **Theory of Hard-Label Attacks.** We provide the first theoretical analysis showing that hard-label black-box attacks, specifically RayS-like methods, can asymptotically match white-box FGSM. Our analysis identifies search dimensionality and cumulative sign-estimation errors as the primary bottlenecks limiting practical efficiency.
- **Prior-Guided Initialization:** We propose a zero-query initialization strategy grounded in image frequency statistics. Unlike blind random sampling, this method leverages prior

knowledge to locate a starting point with a smaller decision boundary distance and better alignment with the true gradient sign.

- **Pattern-Driven Optimization (PDO):** We design the PDO method, which reduces the search space and mitigates the gain cancellation effect inherent in baseline equal-partitioning search. We provide theoretical guarantees on its improved query complexity and experimentally demonstrate its faster convergence and higher cosine similarity with the true gradient sign.
- **SOTA Performance:** Extensive experiments demonstrate that our proposed DPAttack significantly outperforms existing algorithms in terms of ASR and query efficiency. It proves highly effective against traditional DNNs, foundation models (e.g., CLIP), and real-world APIs, while successfully bypassing SOTA defenses like Blacklight.

2 Related Work

2.1 Problem Formulation & Background

Given a victim model $\mathcal{F} : \mathbb{R}^d \rightarrow \{1, \dots, M\}$ (where M denotes the number of classes), a clean image $\mathbf{x} \in \mathbb{R}^d$, and its ground-truth (GT) label y , an untargeted adversarial attack aims to generate an adversarial example (AE) $\mathbf{x}^* = \mathbf{x} + \Delta$ such that $\mathcal{F}(\mathbf{x}^*) \neq y$. The objective is to maximize the classification loss $\mathcal{L}(\mathbf{x} + \Delta, y)$ while constraining the perturbation magnitude within an allowed ℓ_p -ball (typically $p \in \{2, \infty\}$) of radius ϵ . Formally:

$$\max_{\Delta} \mathcal{L}(\mathbf{x} + \Delta, y), \quad \text{s.t.} \quad \|\Delta\|_p \leq \epsilon. \quad (1)$$

White-box vs. Black-box. In white-box settings, attackers optimize Eq. (1) using gradients, e.g., the Fast Gradient Sign Method (FGSM) [28]: $\mathbf{x}' = \mathbf{x} + \epsilon \cdot \text{sgn}(\nabla \mathcal{L}(\mathbf{x}, y))$. However, in the *hard-label black-box* setting, the attacker only accesses the top-1 predicted label, rendering direct gradient access impossible.

2.2 Hard-Label Black-Box Attacks

Early research, such as the Boundary Attack [6], relied on heuristic random walks along the decision boundary. While pioneering, it suffered from extremely low query efficiency due to the blindness of its search strategy. To improve convergence, subsequent works incorporated gradient or normal vector estimation to guide the attack. Canonical methods like HSJA [8] and Bounce [54] utilize Monte Carlo sampling to approximate the decision boundary normal, enabling more directed perturbation updates. Building on this, TtBA [56] weights the perturbation direction with its estimated normal vector. It utilizes a robust “two-third” update rule and curvature-based detection to escape local optima, achieving superior efficiency in normal-vector-based attacks.

However, these gradient-estimation-based methods typically require substantial query budgets to approximate normal vectors. Distinct from this direction, a parallel line of optimization-based approaches bypasses explicit normal estimation. Opt [12] pioneered this by formulating the attack as a zero-order optimization task. In line with this approach, SignOpt [11] further improved query efficiency by reconstructing the gradient direction solely from the

aggregated signs of directional derivatives along random projections, rather than estimating magnitude. Specifically, SignOpt reformulates the attack objective in Eq. (1) as finding a unit vector $\mathbf{v} \in \mathbb{S}^d$ (where \mathbb{S}^d is a unit sphere) to minimize:

$$g(\mathbf{v}) = \min\{r > 0 \mid \mathcal{F}(\mathbf{x} + r \cdot \mathbf{v}) \neq y\}. \quad (2)$$

Here, $g(\cdot)$, defined on \mathbb{S}^{d-1} , represents the shortest distance r from the clean image \mathbf{x} to the decision boundary along direction \mathbf{v} . SignOpt solves Eq. (2) by estimating the gradient $\nabla_{\mathbf{v}} g(\mathbf{v})$ and updating \mathbf{v} using standard Stochastic Gradient Descent (SGD)² as follows:

1. Sample multiple directions $\{\mathbf{n}_i\}_{i=1}^N$ from a Gaussian distribution, typically setting $N = 200$ to mitigate noise.
2. Obtain the sign of the directional derivative via finite differences³: $\text{sgn}(\nabla_{\mathbf{n}_i} g(\mathbf{v})) = \text{sgn}([g(\mathbf{v} + \tau \mathbf{n}_i) - g(\mathbf{v})]/\tau)$, where τ is a small constant.
3. Approximate $\nabla_{\mathbf{v}} g(\mathbf{v}) \approx \sum_{i=1}^N \text{sgn}(\nabla_{\mathbf{n}_i} g(\mathbf{v})) \cdot \mathbf{n}_i$ and update \mathbf{v} using SGD with a learning rate η .

Despite these advancements, continuous gradient-recovery approaches still struggle with high-dimensional search spaces, particularly under ℓ_{∞} constraints. This limitation motivated the development of discrete search strategies, which we detail below.

2.3 Discrete Hard-Label Attacks

Different from the aforementioned methods that attempt to approximate continuous gradients, a distinct category of attacks, represented by RayS [7] and ADBA [55], abandons explicit gradient estimation entirely. Instead, these methods directly search for the optimal perturbation direction within a discrete space (i.e., $\{-1, 1\}^d$), leveraging the empirical observation that ℓ_{∞} -bounded adversarial perturbation often lies on the vertices of the ℓ_{∞} ball [43] to accelerate the search process. As our proposed framework follows and improves upon this discrete search paradigm, we review these two baselines in detail.

RayS [7]. RayS converts continuous optimization into a discrete search problem over $\mathcal{H} \equiv \{-1, +1\}^d$. To this end, its optimization objective is:

$$\min_{\mathbf{d} \in \mathcal{H}} g(\mathbf{d}) \quad \text{where } \mathcal{H} \equiv \{-1, +1\}^d. \quad (3)$$

Naive RayS (NRayS) heuristically optimizes Eq. (3) by flipping the sign of each dimension in the search space \mathcal{H} , while maintaining and updating the minimum perturbation magnitude $g(\mathbf{d}_{\text{best}})$ and its corresponding direction \mathbf{d}_{best} . It initializes the direction as an all-one vector, i.e. $\mathbf{d}_{\text{best}} = \mathbf{d}_0 = \mathbf{1}$, and identifies $g(\mathbf{d}_0)$ via binary search.

To circumvent the inefficiency of dimension-wise flipping in NRayS, the authors proposed Hierarchical RayS (HRayS). HRayS iteratively refines \mathbf{d}_{best} through a hierarchical dyadic structure, effectively exploiting spatial correlations in image gradients [30].

Step 1. Index partitioning. At each hierarchy level $l \in \{1, 2, \dots, \lceil \log_2 d \rceil\}$, the index set $\Gamma = \{1, 2, \dots, d\}$ of vector \mathbf{d}_{best} is sequentially partitioned into 2^l disjoint subsets $\{B_1^{(l)}, B_2^{(l)}, \dots, B_{2^l}^{(l)}\}$ of equal length $d/2^l$.

²The minimization over r is performed using a binary search.

³Note that calculating this directional derivative only requires access to the hard-label oracle $\mathcal{F}(\mathbf{x} + r\mathbf{v}) \neq y$.

Step 2. Sign flipping and direction update. For each subset $B_k^{(l)}$ ($k \in [1, 2^l]$), the signs of the entries in \mathbf{d}_{best} corresponding to this subset are flipped, yielding a perturbed direction $\mathbf{d}_k^{(l)}$. The current best direction \mathbf{d}_{best} is updated *only if* the flipped direction yields a smaller boundary distance. That is

$$\mathbf{d}_{\text{best}} = \begin{cases} \mathbf{d}_k^{(l)} & \text{if } g(\mathbf{d}_k^{(l)}) < g(\mathbf{d}_{\text{best}}) \\ \mathbf{d}_{\text{best}} & \text{Otherwise.} \end{cases} \quad (4)$$

After traversing all 2^l subsets, $B_{k_s}^{(l)}$ is defined as the union of subsets chosen for updating \mathbf{d}_{best} .

Step 3. Refinement. Steps 1 and 2 are repeated by increasing l by 1, progressively refining the direction at finer granularities, until $l = \lceil \log_2 d \rceil$, the query limit is reached, or $g(\mathbf{d}_{\text{best}})$ satisfies the perturbation budget.

ADBA [55]. As the current SOTA for untargeted ℓ_∞ attacks, ADBA follows the hierarchical structure of RayS but identifies a critical inefficiency: RayS relies on binary search to calculate precise boundary distances $g(\cdot)$ for every candidate, which is query-expensive. ADBA improves this by comparing *pairs* of search directions.

Step 1. Index Partitioning: Identical to Step 1 in HRayS.

Step 2. Sign flipping and direction update. For each pair of adjacent subsets $(B_{2k-1}^{(l)}, B_{2k}^{(l)})$ where $k \in [1, 2^{l-1}]$, the signs of entries in \mathbf{d}_{best} (initialized as $\mathbf{d}_0 = \mathbf{1}$) corresponding to these two groups are flipped respectively, yielding two candidate directions $\bar{\mathbf{d}}_1$ and $\bar{\mathbf{d}}_2$. A comparative function $\Lambda(\cdot, \cdot)$ determines which direction is closer to the boundary only when both candidates are adversarial:

$$\mathbf{d}_{\text{best}} = \begin{cases} \mathbf{d}_{\text{best}} & \text{if } \mathcal{F}(\mathbf{x} + r\bar{\mathbf{d}}_1) = y \& \mathcal{F}(\mathbf{x} + r\bar{\mathbf{d}}_2) = y \\ \bar{\mathbf{d}}_1 & \text{if } \mathcal{F}(\mathbf{x} + r\bar{\mathbf{d}}_1) \neq y \& \mathcal{F}(\mathbf{x} + r\bar{\mathbf{d}}_2) = y \\ \bar{\mathbf{d}}_2 & \text{if } \mathcal{F}(\mathbf{x} + r\bar{\mathbf{d}}_1) = y \& \mathcal{F}(\mathbf{x} + r\bar{\mathbf{d}}_2) \neq y \\ \Lambda(\bar{\mathbf{d}}_1, \bar{\mathbf{d}}_2) & \text{Otherwise,} \end{cases} \quad (5)$$

where r denotes the current minimal perturbation distance (initialized to 1 for $[0, 1]$ -valued images), and $\Lambda(\cdot, \cdot)$ returns the direction with the smaller decision boundary distance. The function Λ iteratively checks whether perturbing \mathbf{x} by a gradually reduced r along both $\bar{\mathbf{d}}_1$ and $\bar{\mathbf{d}}_2$ maintains adversarial status. This process stops at r^* if a direction fails to produce an AE or a step limit (e.g., 8) is reached. After determining \mathbf{d}_{best} and updating r to r^* , the algorithm returns to Step 1.

Step 3. Refinement. Identical to Step 3 in HRayS.

Limitation: Although ADBA substantially improves query efficiency over RayS, it relies on a naive all-ones initialization ($\mathbf{d}_0 = \mathbf{1}$), which limits its starting efficiency. More importantly, ADBA remains a purely empirical method that lacks theoretical guarantees regarding its convergence or gradient approximation accuracy. In contrast, our work establishes a theoretically grounded framework that combines a frequency-guided initialization with a structured, pattern-aware optimization strategy, yielding both stronger guarantees and higher practical efficiency.

3 Theoretical Foundations: From Discrete Search to Gradient Sign Estimation

To address the lack of theoretical guarantees in hard-label attacks, we draw inspiration from their soft-label counterparts like SignHunter [1]. While SignHunter is proven to approximate FGSM, its

proof relies on score-based derivative estimation, which is unavailable in hard-label settings. To bridge this gap, we establish a novel theoretical framework demonstrating that RayS-based algorithms (specifically NRayS and HRayS) asymptotically approximate FGSM. As ADBA is a derivative of these core algorithms, our analysis focuses on the fundamental RayS mechanism. We begin by deriving a probabilistic lower bound for the alignment between a random binary vector and the true gradient sign. This provides a key building block for understanding why discrete sign-search methods can recover meaningful gradient information in high dimensions.

THEOREM 1 (APPROXIMATION LOWER BOUND FOR NRAYS).

Let $\mathbf{u} \in \mathbb{S}^{d-1}$ be an arbitrary unit vector. Let $\{\mathbf{d}_j\}_{j=1}^m$ be m vectors sampled independently and uniformly from the binary hypercube $\mathcal{H} \equiv \{-1, +1\}^d$, and let $\hat{\mathbf{d}}_j = \mathbf{d}_j / \sqrt{d}$ be their normalized counterparts. For any precision $\zeta \in (0, 1)$ and confidence $\delta \in (0, 1)$, there exists a constant $C \geq 1$ such that if the sample size satisfies $m \geq -(\ln \delta) e^{Cd\zeta^2}$, then with probability at least $1 - \delta$, there exists at least one index $j \in \{1, \dots, m\}$ satisfying:

$$\mathbf{u}^\top \hat{\mathbf{d}}_j \geq \zeta. \quad (6)$$

Proof. See Appendix A. By instantiating Theorem 1 with the normalized gradient $\mathbf{u} = \nabla \mathcal{L} / \|\nabla \mathcal{L}\|_2$, we conclude that NRayS, given a sufficient query budget m , guarantees finding a direction $\mathbf{d} \in \mathcal{H}$ that aligns with the true gradient $\nabla \mathcal{L}$ with high probability, thereby approximating the FGSM update. While the theoretical bound implies high query complexity (e.g., assuming $C = 1$, ensuring $\zeta \geq 0.1$ with 50% probability on $3 \times 32 \times 32$ sized CIFAR-10 [34] images requires $m \approx 1.5^{13}$ queries), empirical findings from SignHunter suggest that strict gradient alignment is unnecessary. In practice, partial alignment—recovering the signs of the top 20–30% of gradients—suffices to achieve attack success rates exceeding 70% on datasets like CIFAR-10 and ImageNet [16].

Theorem 1 establishes the theoretical feasibility of using discrete search to approach the true gradient sign. However, purely random search remains inefficient in high-dimensional spaces. Extending this insight, Theorem 2 demonstrates how HRayS leverages structured estimation to bypass this bottleneck. It shows that HRayS constructs a direction aligned with the gradient sign, where the approximation quality is governed by the subset selection error rather than blind probabilistic sampling.

DEFINITION 1 (SUBSET-WISE DIRECTIONAL DERIVATIVE INFLUENCE). For a selected index subset $B_{k_s}^{(l)}$ at round l of HRayS (following the definition in Step 2 of HRayS; see Sec. 2.3), we define its influence as the cumulative magnitude of the gradient components within that subset:

$$I(B_{k_s}^{(l)}) := \sum_{i \in B_{k_s}^{(l)}} \left| \frac{\partial \mathcal{L}(\tilde{\mathbf{x}}, y)}{\partial \tilde{\mathbf{x}}[i]} \right|_{\tilde{\mathbf{x}}=\mathbf{x}+g(\mathbf{d}_{\text{best}})\mathbf{d}_{\text{best}}}. \quad (7)$$

This metric quantifies the collective contribution of dimensions in $B_{k_s}^{(l)}$ to increasing the loss. Based on this influence measure, we establish the following subset selection guarantee for HRayS.

LEMMA 1. *Under standard regularity conditions (Assumptions 1 and 2), the subset $B_{ks}^{(l)}$ selected by HRayS at round l satisfies:*

$$I(B_{ks}^{(l)}) \geq \max_{B_k^{(l)}} I(B_k^{(l)}) - \eta_l, \quad (8)$$

where η_l represents the selection error bound at round l .

Proof. See Appendix B. This result guarantees that each round of HRayS identifies a high-impact subset, enabling the subsequent analysis of cumulative progress in the following theorem.

THEOREM 2 (GRADIENT APPROXIMATION GUARANTEE FOR HRAYS). *Assume that the gradient magnitude is uniformly bounded, i.e., $\|\nabla \mathcal{L}(\mathbf{x}, y)\|_\infty \leq G_{\max}$. Let η_l denote the maximum deviation between the directional derivative influence of the subset $B_{ks}^{(l)}$ selected by HRayS at round l and that of the optimal subset $\arg \max_{B_k^{(l)}} I(B_k^{(l)})$. Let $\hat{\mathbf{d}}^*$ be the final direction produced by HRayS. Then, the alignment between $\hat{\mathbf{d}}^*$ and the true gradient sign satisfies*

$$\text{sgn}(\nabla \mathcal{L}(\mathbf{x}, y))^\top \hat{\mathbf{d}}^* \geq \frac{\|\nabla \mathcal{L}(\mathbf{x}, y)\|_1}{G_{\max}} \cdot (1 - \omega), \quad (9)$$

where $\omega = \sum_{l=1}^{\lceil \log_2 d \rceil} \eta_l \|\nabla \mathcal{L}(\mathbf{x}, y)\|_1^{-1}$ denotes the cumulative relative error induced by suboptimal subset selections across all hierarchical rounds.

Proof. See Appendix B. Theorem 2 reveals that although HRayS does not explicitly estimate the gradient, its hierarchical decision mechanism effectively mimics the selection of dimensions with the steepest ascent. By progressively refining the coordinate set, HRayS constructs a direction $\hat{\mathbf{d}}^*$ that closely aligns with $\text{sgn}(\nabla \mathcal{L}(\mathbf{x}, y))$, provided the selection error ω remains small.

Implications for Our Approach. Theorems 1 and 2 collectively suggest that the efficiency of hard-label attacks hinges on two factors: (1) the dimensionality of the search space (which dictates the probability bound in Theorem 1), and (2) the cumulative selection error during structured search (quantified by ω in Theorem 2). Motivated by these theoretical insights, we propose DPAttack, which bridges these gaps through two principled design choices:

Principled Initialization (Sec. 4.3): To mitigate the high dimensionality penalty, we utilize frequency-domain priors to design a zero-query initialization. Crucially, unlike random noise, this frequency-based direction naturally exhibits local spatial coherence (i.e., continuous blocks of consistent signs), effectively reducing the search complexity from the full pixel space to a structured subspace. Theorem 3 also theoretically guarantees that this method yields a positive expected alignment with the true gradient.

Pattern-Driven Optimization (Sec. 4.4): To address the cumulative error ω (Theorem 2), we identify that the fixed, blind partitioning used in RayS and ADBA often disrupts the spatial coherence established by our initialization, leading to conflicting updates (gain cancellation). To resolve this, we employ a tailored pattern-driven search that groups pixels based on their initial sign coherence. By respecting the gradient's intrinsic structure, this strategy is theoretically proven to dominate the baseline in sign alignment (Theorem 4) and reduce query complexity (Theorem 5).

Algorithm 1 DPAttack Process

Input: Target classifier \mathcal{F} , clean RGB image \mathbf{x} , GT label y , perturbation constraint ϵ , candidate block size set \mathbb{W} .

Output: Adversarial example \mathbf{x}^* .

- 1: Obtain optimal block size w and initialization direction \mathbf{d}_n via Dynamic Blocksize Selection: $(w, \mathbf{d}_n, r) \leftarrow \text{DBS}(\mathcal{F}, \mathbf{x}, y, \mathbb{W})$ {refer to Alg. 2}
- 2: Initialize low-pass filtered direction $\phi(\hat{\mathbf{d}}_r)$ with $h \leftarrow w$.
- 3: Perform initial direction selection and boundary search:
- 4: $(\mathbf{d}_0, r_0) \leftarrow \text{BiLiSearch}(\mathcal{F}, \mathbf{d}_n, \phi(\hat{\mathbf{d}}_r), \mathbf{x}, y, r)$ {refer to Alg. 3}
- 5: Set current best parameters: $\mathbf{d}_{\text{best}} \leftarrow \mathbf{d}_0$ and $r \leftarrow r_0$.
- 6: **while** Query Budget > 0 **and** $r > \epsilon$ **do**
- 7: Update \mathbf{d}_{best} and r via Pattern-Driven Optimization (refer to Sec. 4.4).
- 8: **end while**
- 9: **return** $\mathbf{x}^* \leftarrow \text{clip}(\mathbf{x} + r \cdot \mathbf{d}_{\text{best}}, [0, 1])$

4 Our Proposed Attack

4.1 Threat Model

We align our threat model with standard hard-label black-box adversarial attack settings [7], defined by the following aspects:

Adversary's Goal. The adversary aims to generate an untargeted adversarial example \mathbf{x}^* that misclassifies the victim model (i.e., $\mathcal{F}(\mathbf{x}^*) \neq y$) while maintaining the perturbation within an imperceptible budget (e.g., satisfying the ℓ_∞ or ℓ_2 -norm constraint). Formally, we adopt the same optimization objective as RayS (defined in Eq. (3) in Sec. 2), minimizing the distance to the decision boundary within the discrete search space.

Adversary's Knowledge and Capabilities. We assume a hard-label black-box scenario. The adversary can only interact with the victim model \mathcal{F} via an oracle (e.g., an online API) to obtain the top-1 predicted label for a given input. Access to the model's architecture, parameters, gradients, or continuous output probabilities (soft labels) is strictly prohibited.

4.2 The Overall Attack Pipeline of DPAttack

Guided by the theoretical insights established in Sec. 3, we propose DPAttack, a coarse-to-fine framework designed to efficiently approximate the optimal gradient sign. As illustrated in Fig. 2 and Algorithm 1, the pipeline consists of two integrated stages: (1) The Dynamic Decision-Making (DDM) Module (Sec. 4.3), which leverages frequency priors to generate a structured and informative initialization; and (2) The Pattern-Driven Optimization (PDO) Module (Sec. 4.4), which refines this direction by exploiting spatial coherence to accelerate convergence. We detail these components below.

4.3 Better Initialization via Dynamic Decision-Making (DDM)

Our initialization approach relies on the premise that profiling model vulnerabilities provides effective prior knowledge for constructing potent initial perturbations. While previous studies [9] have used Shapley values to identify frequency sensitivity, this metric is derived by masking frequency bands rather than perturbing them, making it ill-suited for capturing sensitivity to additive noise. To address this, we introduce a novel analysis method and subsequently propose the DDM module.

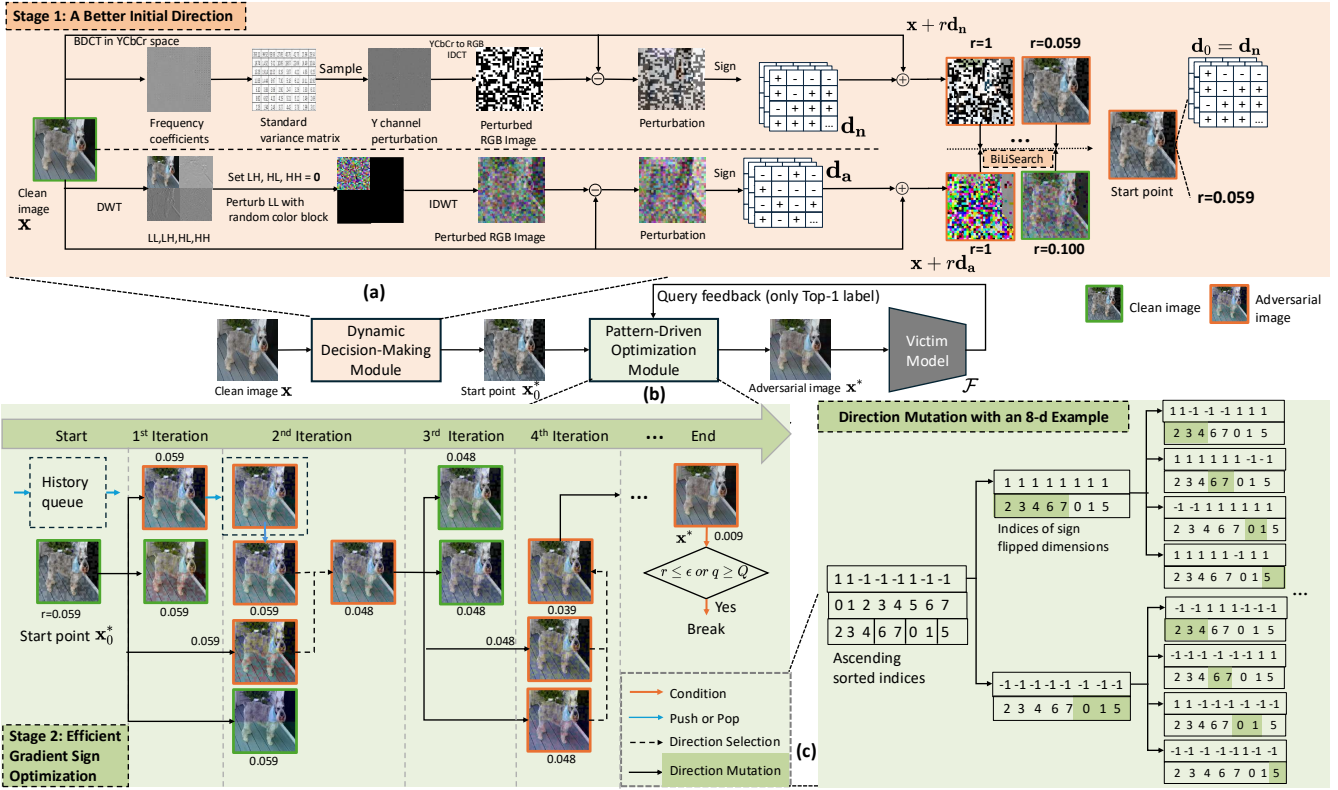


Figure 2: Framework of the proposed hard-label attack method DPAttack. (a) Stage 1: The Dynamic Decision-Making (DDM) module generates a superior initial perturbation direction d_0 . (b) Stage 2: The Pattern-Driven Optimization (PDO) module iteratively refines the direction and the perturbation magnitude r , yielding the final adversarial example $\mathbf{x}^* = \text{clip}(\mathbf{x} + r \hat{\mathbf{d}}^*, [0, 1])$.

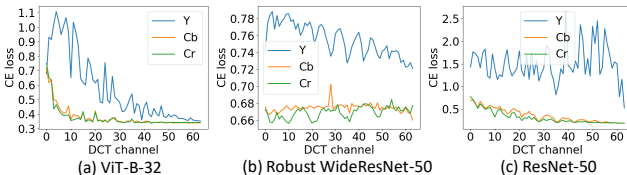


Figure 3: Classification sensitivity analysis of frequency bands via the proposed BFS. Higher CE loss indicates greater sensitivity of the corresponding BDCT frequency band. The BDCT block size is set to $w = 8$.

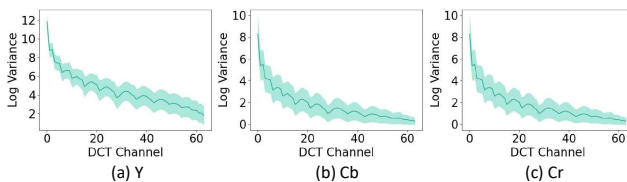


Figure 4: Clean image frequency statistics. The solid line and the shaded region represent the mean and standard deviation of the log-variance $\log(\sigma_{c,i,j}^2 + 1)$ (defined in Eq. (11)).

4.3.1 Analysis: Block-DCT [53] Frequency Sensitivity (BFS). To accurately characterize model vulnerability to frequency-based noise, we propose BFS. While drawing conceptual inspiration from the frequency sensitivity analysis in [62], our method significantly advances this framework by introducing two critical modifications tailored for adversarial efficiency: 1) We employ the variation in CE loss rather than classification error rate to provide a fine-grained sensitivity metric; 2) We apply perturbations in the Block Discrete Cosine Transform (BDCT) domain [53] instead of the Fast Fourier Transform domain [22], as DNNs are typically more vulnerable to the block-wise artifacts introduced by BDCT.

BFS Procedure. Given an RGB image $\mathbf{x} \in \mathbb{R}^{C \times H \times W}$, we convert it to YCbCr space and divide it into non-overlapping blocks of size $w \times w$ (e.g., $w = 8$). Performing DCT on these blocks yields the frequency matrix $\mathbf{I} \in \mathbb{R}^{C \times Z \times w \times w}$, where $Z = (H/w) \times (W/w)$ is the total number of blocks. To measure sensitivity, we define a Gaussian noise distribution $\mathcal{N}(0, \sigma_{\max}^2)$, where σ_{\max} is calibrated such that the perturbation exhausts the pixel-domain budget ϵ . For a specific frequency coordinate (c, i, j) , we sample a noise vector $\hat{\mathbf{w}}_{c,i,j} \in \mathbb{R}^Z$ from this Gaussian distribution and add it to the corresponding coefficients across all blocks. The perturbed image $\hat{\mathbf{x}}$ is obtained via Inverse BDCT (IBDCT) and projection:

$$\hat{\mathbf{x}} = \Pi_{\epsilon, \mathbf{x}}(\text{IBDCT}(\mathbf{I}[c, :, i, j] + \hat{\mathbf{w}}_{c,i,j}, w)) \quad (10)$$

Table 1: Pearson correlation analysis (\bar{r} - p -value) between the proposed BFS profile and the clean image frequency variance across different models and color channels.

Channel	ViT-B-32	Robust WideResNet-50	ResNet-50
Y	0.8074 ^{7.69E-16}	0.7024 ^{9.87E-11}	0.0327 ^{7.97E-01}
Cb	0.9274 ^{3.61E-28}	-0.1714 ^{1.76E-01}	0.9137 ^{6.18E-26}
Cr	0.8844 ^{3.44E-22}	-0.4087 ^{7.99E-04}	0.9618 ^{1.40E-36}

¹ \bar{r} : the correlation coefficient; p -value: the statistical significance.

where $\Pi_{\epsilon, \mathbf{x}}(\cdot)$ denotes the projection operator that maps the input onto a hypersphere centered at \mathbf{x} with radius ϵ .

Observation: The Correlation with Clean Image Statistics. We applied BFS to 1,000 ImageNet validation images across diverse architectures. Results on ResNet-50, ViT-B-32, and adversarially trained WideResNet-50 (Fig. 3) reveal that model sensitivity (CE loss) exhibits an oscillatory decay from low to high frequencies.

Crucially, we observe that this sensitivity pattern is closely related to the frequency-domain variance of clean images. We compute the standard deviation of frequency coefficients across blocks for clean images as:

$$\sigma_{c,i,j} = \sqrt{\frac{1}{Z} \sum_{z=0}^{Z-1} |\mathbf{I}[c, z, i, j] - \mu_{c,i,j}|^2}. \quad (11)$$

As shown in Fig. 4, the distribution of $\sigma_{c,i,j}$ exhibits a similar decaying trend. To quantitatively assess this relationship, we compute the Pearson correlation between the channel-wise BFS sensitivity curves and the corresponding clean-image frequency variance profiles. As summarized in Table 1, we observe a strong and statistically significant positive correlation across standard architectures such as ViT-B-32 and ResNet-50. For adversarially trained models, this positive correlation remains evident in the luminance channel (Y) (e.g., $\bar{r} \approx 0.7$), while the chrominance channels exhibit more heterogeneous or mildly negative correlations. Importantly, this does not alter the overall trend, since the sensitivity of chrominance channels is consistently much lower than that of the luminance channel across all models, as reflected by their substantially smaller CE responses.

While targeting model-specific sensitivity peaks (BFS-peak) may ideally seem optimal, identifying the exact band is almost infeasible in black-box settings where the architecture is unknown. Moreover, empirical evidence (App. D.1) reveals that compared to clean-image statistics, BFS-peak yields only marginal gains on matched models while suffering severe degradation on mismatched ones. Therefore, we leverage the intrinsic frequency properties of clean images to establish a practical, model-agnostic prior.

4.3.2 Methodology: Constructing Initial Directions. Based on the observation above, we propose using the clean image frequency variance $\sigma_{c,i,j}$ directly as a prior to construct an initialization direction \mathbf{d}_n . For comparison and diversity, we also introduce two alternative directions, \mathbf{d}_b and \mathbf{d}_r , based on gradient local similarity [30] and color sensitivity [2].

1. Variance-Based Direction (\mathbf{d}_n). Specifically, we construct the frequency perturbation matrix $\tilde{\Delta}$ by sampling noise coefficients

Table 2: Comparison of curvature (κ) and perturbation distances (ℓ_∞ , ℓ_2) across initialization methods. “Image” denotes a random sample from a different class.

Metrics	Curvature $\kappa \uparrow$		$\ell_\infty \downarrow$		$\ell_2 \downarrow$	
	Methods	Avg.	Med.	Avg.	Med.	Avg.
Gaussian	58,736	49,404	0.363	0.341	49.4	46.7
Uniform	58,273	48,932	0.315	0.318	49.7	48.6
Image	57,873	47,068	0.362	0.364	55.2	54.2
RayS	58,167	45,454	0.518	0.533	147.8	150.1
ADBA	39,408	33,592	0.354	0.339	114.9	121.2
Our \mathbf{d}_r	58,308	47,349	<u>0.091</u>	0.083	<u>35.1</u>	32.1
Our \mathbf{d}_b	60,934	50,192	0.108	<u>0.072</u>	39.3	<u>27.2</u>
Our \mathbf{d}_n	68,502	54,743	0.078	0.069	28.9	26.1

$\mathbf{w}_{c,i,j} \sim \mathcal{N}(0, \sigma_{c,i,j}^2)$ for each frequency band. The spatial perturbation direction is then derived by:

$$\mathbf{x}'_n = \text{IBDCT}(\mathbf{I} + \tilde{\Delta}, \mathbf{w}), \quad \mathbf{d}_n = \text{sgn}(\mathbf{x}'_n - \mathbf{x}), \quad \text{with } \text{sgn}(0) := 1. \quad (12)$$

Zero elements in \mathbf{d}_n are replaced with 1 to maintain a dense search space. This initialization method is efficient as it requires no model queries or pre-training.

2. Gradient-Similarity-Based Direction (\mathbf{d}_b). Inspired by HRayS, we verify that gradient spatial correlations persist even after sign quantization (Fig. 5 (a)). To leverage this sign-level coherence, we design \mathbf{d}_b as a block-wise structure consisting of \hat{m} segments of length \hat{n} , where each segment is assigned a uniform sign:

$$\mathbf{d}_b = \left((-1)^{\lfloor (i-1)/\hat{n} \rfloor} \right)_{i=1}^{\hat{m}}. \quad (13)$$

3. Square-Color-Based Direction (\mathbf{d}_r). Leveraging the sensitivity of DNNs to square-shaped color perturbations [2], we generate \mathbf{d}_r as the sign of the residual between the clean image \mathbf{x} and a randomly square-perturbed image \mathbf{x}'_r , where the square has side length h . That is:

$$\mathbf{d}_r = \text{sgn}(\mathbf{x}'_r - \mathbf{x}), \quad \text{with } \text{sgn}(0) := 1. \quad (14)$$

More detailed formulation of generating \mathbf{x}'_r is presented in App. E. **Low-Frequency Focusing Method (ϕ).** To mitigate mutual interference across frequency bands, we introduce a wrapper function $\phi(\cdot)$ that confines perturbations to the low-frequency component \mathbf{x}_{LL} via Discrete Wavelet Transform (DWT) [22]. We prioritize DWT over BDCT here to minimize hyperparameters, reserving BDCT specifically for generating pixel-domain block-wise artifacts. We extract the low-pass component $\mathbf{x}_{LL} \in \mathbb{R}^{C \times \hat{H} \times \hat{W}}$ via:

$$\mathbf{x}_{LL}, \mathbf{x}_{\text{others}} = \text{DWT}(\mathbf{x}, dl), \quad (15)$$

where $\hat{H} = H/2^{dl}$ and $\hat{W} = W/2^{dl}$. The decomposition level dl is bounded by $\lfloor \log_2(\bar{w}) \rfloor$, where \bar{w} represents the pattern size of the underlying strategy (i.e., w for \mathbf{d}_n , \hat{n} for \mathbf{d}_b , or h for \mathbf{d}_r).

We isolate low frequencies by setting the residuals $\mathbf{x}_{\text{others}} = \mathbf{0}$ and applying a perturbation $\hat{\mathbf{d}}_a \in \{\hat{\mathbf{d}}_n, \hat{\mathbf{d}}_b, \hat{\mathbf{d}}_r\}$ to \mathbf{x}_{LL} . Note that $\hat{\mathbf{d}}_a$ is generated with pattern size scaled by 2^{-dl} (e.g., $w/2^{dl}$ for $\hat{\mathbf{d}}_n$). The perturbed low-frequency component $\hat{\mathbf{x}}_{LL} = \mathbf{x}_{LL} + \hat{\mathbf{d}}_a$ is then projected back to the pixel space via Inverse DWT:

$$\mathbf{x}'_a = \text{IDWT}(\hat{\mathbf{x}}_{LL}, \mathbf{0}, dl). \quad (16)$$

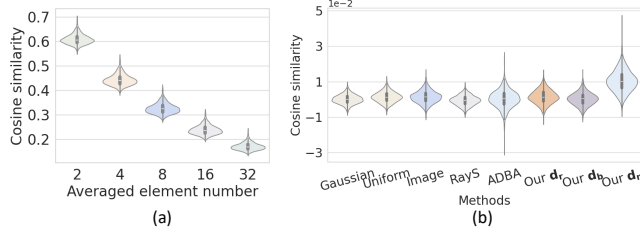


Figure 5: (a) Cosine similarity between the true gradient sign $\text{sgn}\nabla\mathcal{L}(x, y)$ and its block-wise averaged approximations. (b) Cosine similarity between the true gradient sign and directions from various initialization methods.

Encapsulating this process as $\phi(\hat{d}_a)$, we derive the final direction d_a by taking the sign of the difference, ensuring non-zero entries:

$$d_a = \text{sgn}(x'_a - x), \quad \text{with } \text{sgn}(0) := 1. \quad (17)$$

4.3.3 Validation and Dynamic Selection. We benchmark our initialization directions against standard baselines (Gaussian, Uniform, RayS, ADBA, and random images) using ResNet-50. The resulting starting points are evaluated visually (App. F) and quantitatively via three metrics: 1) Perturbation distance (ℓ_2/ℓ_∞); 2) Local curvature κ (indicating optimization speed)⁴; and 3) Cosine similarity with the true gradient sign. As detailed in Table 2 and Fig. 5, d_n consistently demonstrates superior geometric properties: it achieves the highest gradient sign alignment (Fig. 5(b)) and significantly smaller boundary distances with higher local curvature compared to all baselines. These advantages are critical for optimization; indeed, our ablation study (Sec. 5.6) confirms that replacing d_n with other initializations severely degrades the attack success rate.

To theoretically justify this advantage, we model initialization as a sign alignment problem. We prove that sampling from a BDCT frequency distribution positively correlated with model sensitivity guarantees a positive expected alignment with the true gradient sign (as formally established in **Theorem 3**), a property lacking in random noise. This result is fundamentally rooted in the Arcsine Law [51] (see App. G for the complete proof), which states that for jointly Gaussian variables, a positive correlation in their values induces a positive correlation in their signs. In our setting, the frequency-variance prior biases the distribution of d_n toward frequency bands that are, on average, more sensitive to the model. This bias is sufficient to induce a strictly positive expected alignment with the true gradient sign. In contrast, isotropic random initialization distributes energy uniformly across all frequencies and therefore yields zero expected alignment. Under the assumption of a local linear decision boundary, this positive alignment further implies a smaller expected boundary distance, as formalized in Corollary 1, providing a theoretical explanation for the empirical advantages of d_n observed in Table 2.

⁴Analysis of optimization behaviors and κ estimation are detailed in App. H and I.

THEOREM 3 (POSITIVE EXPECTED ALIGNMENT UNDER FREQUENCY-VARIANCE PRIOR). Let $x_0 = Uz$ be the initialization generated under Asmp. 4 with sign vector $d_n = \text{sgn}(x_0)$. Let h be the proxy of the gradient constructed in Asmp. 4, and let $u = \text{sgn}(\nabla_x \mathcal{L})$ denote the sign of the true gradient. Under Lemma 4 and Asmp. 5, the channel-wise correlations between x_0 and h induce coordinate-wise correlations between x_0 and u . Then the expected cosine alignment satisfies

$$\frac{1}{d} \mathbb{E}[\langle d_n, u \rangle] = \frac{1}{d} \sum_{i=1}^d \mathbb{E}\left[\frac{2}{\pi} \arcsin(\rho_i)\right] > 0, \quad (18)$$

where $\rho_i = \text{Corr}((x_0)_i, (h)_i)$ is given in Lemma 4. In contrast, for isotropic random initializations d_{rand} , we have

$$\mathbb{E}[\langle d_{\text{rand}}, u \rangle] = 0.$$

Remark. The positivity above holds in expectation and does not require $\rho_i > 0$ for every pixel coordinate.

Adaptive Block Size Selection. While our theoretical analysis supports the use of frequency-based initialization, empirical results (Sec. 5.6) indicate that the attack performance exhibits mild sensitivity to the choice of the BDCT block size for a given victim model. This sensitivity arises because the block size controls the granularity of the frequency decomposition, which in turn affects both the correlation between the initial direction and the true gradient sign, as well as the efficiency of the subsequent optimization process. To account for this variability without manual tuning, we introduce a Dynamic Block Size Selection (DBS) strategy that query-efficiently identifies a suitable block size w (see App. J).

BiLiSearch for Robust Selection. Even with optimized block sizes, relying on a single initialization is not universally optimal against unknown defenses (e.g., adversarial training). While d_n is generally superior, we observe that the color-based alternative $\phi(\hat{d}_r)$ yields marginal gains on adversarially trained models (see Table 9). To ensure robustness, we propose BiLiSearch (App. K), a hybrid strategy combining binary and line search to efficiently select the direction d_0 with the minimal boundary distance r_0 :

$$d_0, r_0 = \text{BiLiSearch}(d_n, \phi(\hat{d}_r)), \quad x_0^* = \text{clip}(x + r_0 d_0, [0, 1]). \quad (19)$$

4.4 Pattern-Driven Optimization (PDO)

Having established the initial direction d_0 , the next challenge is efficient refinement. Unlike random noise, d_0 —derived from BDCT domain analysis—naturally exhibits strong spatial coherence in the pixel space, forming contiguous blocks of identical signs (“runs”), as illustrated in Figs. 2(a) and (c). However, SOTA hard-label attacks such as RayS and ADBA adopt rigid, pattern-agnostic dyadic bisection, which blindly partitions the pixel space and fragments these coherent structures. This mismatch disrupts the intrinsic geometry of d_0 and leads to *gain cancellation* (formally defined in Lemma 5), where conflicting gradient signals within a partition offset each other, resulting in query inefficiency.

To address this issue, we propose the *Pattern-Driven Optimization (PDO)* module, which explicitly aligns the search process with the spatial patterns of d_0 . Instead of operating in the full pixel space of dimension d , PDO treats each sign-consistent run as an atomic

search unit, effectively reducing the optimization problem to a lower-dimensional *pattern space* with dimensionality equal to the number of runs $M \ll d$. For example, on ImageNet ($d \approx 150k$), using block sizes $w \in \{4, 8, 16\}$ reduces M to approximately 20k, 11k, and 6k, respectively. By preserving spatial coherence and avoiding destructive partitioning, PDO enables more efficient gradient sign approximation that scales with the compressed pattern structure rather than the raw pixel dimensionality.

4.4.1 Algorithm Implementation. To operationalize this, PDO constructs a search tree T_{pat} explicitly aligned with the pattern of \mathbf{d}_0 , proceeding in three phases:

Phase 1: Pattern-Driven Tree Construction. We build a hierarchical search tree dynamic to \mathbf{d}_0 :

- (1) **Sorting and Indexing:** Define a permutation Γ sorting \mathbf{d}_0 such that $\mathbf{d}_0[\Gamma(1)] \leq \dots \leq \mathbf{d}_0[\Gamma(d)]$.
- (2) **Atomic Partitioning:** Partition Γ into atomic units $\{B_1, \dots, B_M\}$ grouping contiguous indices, effectively capturing the “runs” in \mathbf{d}_0 .
- (3) **Hierarchical Grouping:** Build a binary hierarchy where, at level $s \in [1, \lceil \log_2 M \rceil]$, atomic units are merged into 2^s groups $\{\mathcal{G}_j\}_{j=1}^{2^s}$ for coarse-to-fine search.

Phase 2: Sign Flipping and Direction Update. We refine \mathbf{d}_{best} (initialized as \mathbf{d}_0) by iteratively flipping signs within adjacent group pairs $(\mathcal{G}_{2l-1}, \mathcal{G}_{2l})$ to generate candidates $\bar{\mathbf{d}}_1$ and $\bar{\mathbf{d}}_2$. To maximize efficiency, we employ a history-aware update rule:

$$\mathbf{d}_{\text{best}} = \begin{cases} \mathbf{d}_{\text{best}} & \text{if } \mathcal{F}(\mathbf{x} + r\bar{\mathbf{d}}_1) = y \& \mathcal{F}(\mathbf{x} + r\bar{\mathbf{d}}_2) = y \\ \Lambda(\bar{\mathbf{d}}_1, \bar{\mathbf{d}}_{\text{his}}) & \text{if } \mathcal{F}(\mathbf{x} + r\bar{\mathbf{d}}_1) \neq y \& \mathcal{F}(\mathbf{x} + r\bar{\mathbf{d}}_2) = y \\ \Lambda(\bar{\mathbf{d}}_2, \bar{\mathbf{d}}_{\text{his}}) & \text{if } \mathcal{F}(\mathbf{x} + r\bar{\mathbf{d}}_1) = y \& \mathcal{F}(\mathbf{x} + r\bar{\mathbf{d}}_2) \neq y \\ \Lambda(\bar{\mathbf{d}}_1, \bar{\mathbf{d}}_2) & \text{Otherwise.} \end{cases} \quad (20)$$

Here, Λ selects the direction with the smaller boundary distance. Notably, we use a buffer $\bar{\mathbf{d}}_{\text{his}}$ to cache solitary successful directions, preserving promising candidates that baseline methods (e.g., ADBA) would discard.

Phase 3: Refinement and Loop. We increment the granularity level s to progressively refine the search.⁵ The complete workflow is visualized in Fig. 2(b).

4.4.2 Theoretical Guarantees. Having defined the algorithm, we now utilize a signal recovery framework to justify why aligning the search tree with initialization patterns (T_{pat}) outperforms standard dyadic trees (T_{dyad}) employed by HRayS and ADBA.

THEOREM 4 (PER-QUERY SIGN ALIGNMENT DOMINANCE).

Let $\mathbf{u} = \text{sgn}(\nabla_{\mathbf{x}} \mathcal{L})$ be the true gradient sign, and let $\mathbf{d}_t \in \{\pm 1\}^d$ be the perturbation direction after t queries. We measure sign alignment using the agreement $A(\mathbf{d}_t, \mathbf{u}) := \frac{1}{d} \sum_{i=1}^d \mathbb{I}\{\mathbf{d}_{t,i} = \mathbf{u}_i\}$. Under the assumptions of local block coherence (Asmp. 6) and a weakly positive initial correlation (Asmp. 7), the expected agreement A_t after t queries satisfies:

$$\mathbb{E}[A_t^{\text{pat}}] \geq \mathbb{E}[A_t^{\text{dyad}}], \quad \forall t \in \mathbb{N}, \quad (21)$$

where pat and dyad denote the pattern-driven strategy and the blind dyadic baseline, respectively.

Proof in App. L. The inequality degenerates to an equality only if \mathbf{d}_0 lacks spatial variation (e.g., $\mathbf{d}_0 = \mathbf{1}$) or aligns perfectly with the dyadic grid. We provide empirical verification of this dominance in Sec. 4.4.3. This per-step advantage scales into a significant improvement in asymptotic query complexity, as formalized in **Theorem 5** (see App. M for the full proof). Throughout Theorem 5, we use the number of tree expansions as a proxy for query complexity. This is justified because, in RayS-style hard-label attacks (including our PDO framework), each node expansion incurs at most a constant number of model queries. Therefore, the asymptotic bounds in Theorem 5 translate directly to query complexity up to constant factors. Also, the complexity T quantifies the cost for *full* sign recovery. In practice, attacks succeed upon achieving *sufficient alignment* (partial recovery); thus, actual consumption is usually lower than T . We attribute this complexity gap to a structural phenomenon we term *Intrinsic Gradient Shattering*, a detailed empirical analysis of which is provided in the following validation.

4.4.3 Empirical Validation. To empirically verify Theorems 4 and 5, we track the cosine similarity between the search direction \mathbf{d}_{best} and the true gradient sign $\text{sgn}(\nabla \mathcal{L}(\mathbf{x}, y))$ (averaged over 1,000 ImageNet images). The results are visualized in Fig. 6. Note that to improve clarity, curves undergo a linearly fitted process, which causes a minor visual divergence at $t = 0$ between “Ours” and “Ours w/o PDO” (using standard dyadic split), even though they originate from the exact same initial direction. The observed trends strongly confirm our theoretical claims:

- The “Ours” curve consistently upper-bounds the baseline “Ours w/o PDO” across architectures. This empirical gap confirms Theorem 4, demonstrating that incorporating initial pattern priors generally yields a better descent direction for any given query budget t .
- The substantial gap between the slow ascent of “Ours w/o PDO” and the steep rise of “Ours” also confirms the complexity divergence predicted by Theorem 5. We attribute this to *Intrinsic Gradient Shattering*—a phenomenon where top-magnitude gradient components, critical for optimization, exhibit rapid spatial oscillation. As visualized by the green lines in Fig. 7, the average sign-consistent block size $|B|$ for these top-2% magnitude gradients collapses to ≈ 1 in CNNs and ≈ 2 in ViTs. This inherent fragmentation triggers two distinct regimes:
 - (i) **Dyadic Collapse:** The rigid partitioning of dyadic strategies is forced into a worst-case scenario by these pixel-level oscillations. This drives the search depth toward the theoretical

⁵A fallback that splits atomic units or re-initializes \mathbf{d}_0 is only triggered in rare low-dimensional cases (e.g., CIFAR-10) and was not observed on higher-resolution datasets such as ImageNet.

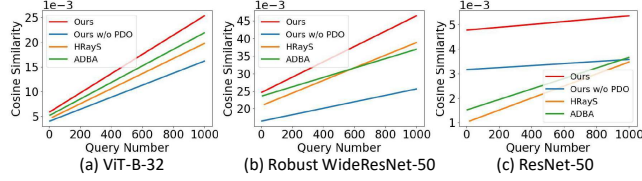


Figure 6: Evolution of cosine similarity between the true gradient sign and the perturbation direction across optimization methods.

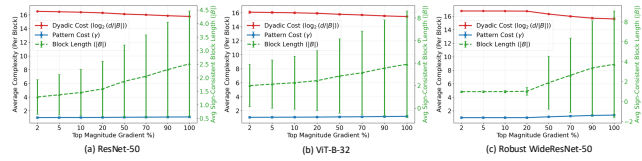


Figure 7: Empirical validation of Theorem 5 across various architectures on ImageNet. Results for additional models are provided in App. Fig. 15.

limit ($\approx \log_2 d$), incurring a query complexity of $\approx 16 \sim 17$ per block—matching the value of dyadic costs in Fig. 7.

- (ii) **Pattern Resilience:** In contrast, PDO sidesteps this shattering by adaptively aligning with the run-length boundaries of \mathbf{d}_0 . By treating these oscillations as coherent atomic units rather than disjoint pixels, PDO maintains a near-optimal fragmentation factor $\gamma \approx 1$ (represented by the blue lines in Fig. 7), significantly accelerating convergence.
- **Comparison with Baselines:** In Fig. 6, our method consistently outperforms HRayS and ADBA. Additionally, the increasing trend of the HRayS curve serves as verification for Theorem 2, confirming that while less efficient than our method, the standard dyadic hierarchy still guarantees a progressive reduction in approximation error.

THEOREM 5 (QUERY COMPLEXITY UNDER BLOCK SIGN-COHERENCE). Under Asmps. 6 and 7, let the true gradient sign \mathbf{u} consist of K spatially coherent blocks $\{B_k\}_{k=1}^K$. To identify descent directions aligned with \mathbf{u} , the expected query complexities for dyadic search (T_{dyad}) and pattern-driven search (T_{pat}) satisfy:

$$T_{\text{dyad}} = \Omega \left(\sum_{k=1}^K \log_2 \frac{d}{|B_k|} \right), \quad T_{\text{pat}} = O \left(\sum_{k=1}^K \gamma_k \right), \quad (22)$$

where γ_k is the number of \mathbf{d}_0 -runs intersecting block B_k . In particular, the pattern-driven strategy is asymptotically more efficient in expectation when $\gamma_k < \log_2(d/|B_k|)$ on average.

5 Evaluation

We evaluate DPAttack against SOTA hard-label attacks across diverse datasets, architectures, and constraints. Our analysis covers standard classifiers (Sec. 5.2), foundation models/APIs (Sec. 5.3), and

robust defenses (Sec. 5.4). We further demonstrate generalization to downstream Object Detection (OD) and segmentation (Sec. 5.5) and provide ablation studies on the initialization, PDO module, the impact of block size w , and the effect of frequency priors (Sec. 5.6).

5.1 Experimental Setup

Datasets. We use CIFAR-10 [34] and ImageNet-1K [16] for standard classification, and ObjectNet [5] to test robustness against context shifts. For downstream tasks, we employ MS-COCO [38] (OD) and SA1B [33] (segmentation). We further include ImageNet-C [27] and PathMNIST [59] to evaluate performance on corrupted and non-natural (biomedical) domains.

Victim Models. For CIFAR-10 and ImageNet-1K, we target representative architectures including ResNet-18/50, ViT-B-32, and DenseNet-121, alongside adversarially trained WideResNet variants [13, 19]. We also evaluate the ViT-H-14 CLIP [29] foundation model. For downstream tasks, we use FasterRCNN [45] (OD) and SAM [33] (segmentation). Evaluations on specialized datasets (ImageNet-C, PathMNIST) utilize domain-specific top-performance models. See App. N for the full list of 15+ evaluated architectures.

Metrics. We evaluate attack effectiveness using Attack Success Rate (ASR) within a maximum query budget (Max.Q). We compute $\text{ASR} = \frac{1}{N} \sum_{i=0}^{N-1} \mathbb{I}(\mathcal{F}(\mathbf{x}_i^*) \neq y_i)$ and set $N = 200$ following [54]. To assess efficiency, we further report the average (Avg.Q) and median (Med.Q) queries among successful attacks.

Baselines and Our Methods. We evaluate two variants of our method: (1) **Ours_{opt}**, which uses the fixed block size that achieves the highest average ASR across budgets, and (2) **Ours_{dyn}**, which employs our dynamic block size selection strategy. We compare them against SOTA query-based hard-label attacks: **TtBA** [56], **HRayS** [7], **ADBA** [55], **HSJA** [8], and **Bounce** [54] with both random (**BouR**) and targeted (**BouT**) initializations. For ℓ_2 comparisons, we include **SurFree** [41] and **Tangent** [39]. Implementation details, including the setting of decomposition level dl and hyperparameter configurations, are provided in Appendix N.

5.2 Performance on Standard Classifiers

We evaluate the efficacy of DPAttack against standard classifiers trained on CIFAR-10, ImageNet-1K, ImageNet-C and PathMNIST. Primary results are summarized in Tables 3, 13-??, where extensive evaluations across diverse architectures and domains are detailed.

ASR. Across nearly all scenarios, our method consistently outperforms SOTA baselines. The gap is particularly pronounced under tight query budgets. For instance, on ResNet-50 with Max.Q= 50, our_{dyn} surpasses the SOTA ADBA by 32.5% in ASR while consuming only approximately two-thirds of its Avg.Q and Med.Q.

Query Efficiency. DPAttack consistently achieves competitive or lower query consumption compared to prior work, while maintaining substantially higher ASR. Although our Avg.Q on ImageNet occasionally exceeds that of BouT, this stems from our significantly higher ASR: we successfully crack “hard” samples that require more queries, whereas baseline methods simply fail on them (yielding no query count contribution). Note that for extremely low budgets (Max.Q < 20), the ASR of Ours_{dyn} drops due to the overhead of its warm-up phase to do dynamic block size selection.

Table 3: The attack performance on ImageNet (ResNet-50) under $\ell_\infty = 0.05$ constraint.

Metrics	ASR								Avg.Q								Med.Q									
	HSJA	BouR	BouT	TtBA	HRayS	ADBA	Ours _{opt}	Ours _{dyn}	HSJA	BouR	BouT	TtBA	HRayS	ADBA	Ours _{opt}	Ours _{dyn}	HSJA	BouR	BouT	TtBA	HRayS	ADBA	Ours _{opt}	Ours _{dyn}		
MaxQ	0.0	0.0	<u>3.5</u>	0.0	2.0	0.0	20.5	0.0	0.0	-	5	-	5	-	5	-	-	-	5	-	5	-	5	-	-	
5	0.0	0.0	<u>9.5</u>	0.0	2.0	0.0	37.0	-	-	-	6	-	10	-	6	-	-	-	6	-	10	-	5	-	-	
10	0.0	0.0	<u>17.0</u>	0.0	2.0	0.0	51.5	39.5	14	14	6	-	20	17	6	19	14	14	6	-	20	17	5	19	-	
20	6.5	6.5	<u>17.5</u>	6.5	21.0	38.0	57.0	64.0	40	40	21	75	52	46	24	29	59	59	6	75	56	42	15	20	-	
50	6.0	6.0	<u>17.0</u>	16.5	22.5	51.5	55.0	13	13	20	-	42	32	19	23	13	13	6	-	40	31	13	20	-	-	
80	14.0	14.0	<u>17.5</u>	6.5	21.0	38.0	57.0	40	40	21	75	52	46	24	29	59	59	6	75	56	42	15	20	-	-	
100	15.0	16.0	<u>16.0</u>	7.5	25.0	49.5	62.0	66.0	40	37	23	77	60	56	29	31	59	38	6	75	57	59	15	20	-	-
200	17.5	17.5	<u>22.0</u>	10.5	51.0	71.0	75.5	75.0	75	64	72	87	109	87	49	46	99	99	48	75	104	80	26	22	-	-
300	20.0	18.5	<u>21.0</u>	14.0	54.0	79.5	83.5	83.5	77	71	54	126	136	104	67	66	99	99	6	82	121	84	34	22	-	-
400	16.5	16.0	<u>23.5</u>	16.0	69.0	85.0	88.5	89.0	61	60	72	158	160	117	83	85	99	99	7	144	143	85	38	24	-	-
500	20.5	18.0	<u>25.5</u>	19.0	70.5	87.5	90.0	92.0	92	81	85	184	198	128	88	97	99	99	88	146	174	88	38	29	-	-
1k	20.5	18.5	<u>22.0</u>	32.5	89.5	93.5	95.5	97.5	164	110	184	414	312	163	127	131	150	149	8	404	226	97	44	36	-	-
3k	23.0	19.5	<u>23.0</u>	59.5	97.5	99.0	99.5	100.0	352	209	196	1,117	431	236	199	180	150	149	139	965	252	100	48	39	-	-
5k	21.0	19.0	<u>22.5</u>	67.5	100.0	100.0	100.0	100.0	210	140	319	1,441	522	249	222	180	149	149	138	978	263	102	49	39	-	-

Additional Results. Comparisons under varying perturbation magnitudes and ℓ_2 constraints are provided in Appendix O.1 and Appendix P, respectively. These results consistently demonstrate our method’s superior ASR and query efficiency over SOTA baselines; notably, Ours_{dyn} excels in ℓ_2 scenarios, often significantly surpassing the Ours_{opt} version.

5.3 Performance on CLIP and Commercial APIs

CLIP. CLIP model is a versatile and prevailing foundation vision-language model for many downstream tasks and is suitable for zero-shot image classification, which achieves 77.4% Top-1 classification accuracy on ObjectNet. We evaluate our method against the CLIP model on ObjectNet to test its zero-shot robustness. To strictly simulate a hard-label black-box setting, we assume the adversary can only access the index of the predicted category (the class with the highest cosine similarity), without access to the specific similarity values or gradients. As shown in Table 4, our method demonstrates superior ASR and query efficiency compared to SOTA baselines. Notably, under a tight query budget (Max.Q= 50), Ours_{dyn} outperforms ADBA by 32% in ASR while halving the queries. Even with a generous budget ($> 3,000$), while the ASR gap narrows ($< 10\%$), our method remains significantly more efficient, reducing Med.Q by approximately 80% and Avg.Q by 40% compared to ADBA.

APIs. We further validate our approach on four popular commercial image labeling services: Imagga [31], Google Cloud Vision [23], Tencent DetectLabel Pro [49], and Baidu General Image Recognition [4]. The test images are randomly sampled from the ImageNet validation set. Due to the high cost of commercial API calls, we compare exclusively against ADBA, the strongest baseline identified in previous experiments. The results, summarized in Table 5, indicate that our algorithm consistently outperforms ADBA across all APIs and perturbation limits. For instance, on the Tencent API with $\ell = 0.1$, Ours_{opt} achieves an ASR improvement of over 44% while consuming significantly fewer queries. Our method drastically reduces the query complexity from the tens or hundreds required by ADBA to merely 10 – 20. This significant reduction in attack cost exposes the severe vulnerability of online APIs to low-budget adversaries, highlighting the urgent need for more robust defenses.

5.4 Performance on Defensive Methods

We evaluate the robustness of our attack against both static defense (adversarial training) and dynamic stateful defense mechanisms.

Adversarial Training. We test attack effectiveness on robust WideResNet models trained on CIFAR-10 and ImageNet. As summarized in Table 6, our method achieves the highest ASR while maintaining superior query efficiency. Specifically, we outperform HRayS in ASR by over 7% on ImageNet. In contrast, ADBA shows limited improvement (0.5% on ImageNet) and even degradation (-0.5% on CIFAR-10) compared to HRayS. Additional results under various perturbation constraints are detailed in Appendix O.3.

Stateful Detection (Blacklight). We extend our evaluation to Blacklight [37], a SOTA defense that detects attacks by identifying highly correlated queries via hashing-based fingerprinting. Since Blacklight flags attacks when hash collisions within a sliding window exceed a threshold, we propose a randomized variant of DPAttack to break this correlation. Specifically, we inject Gaussian noise ξ into the update direction: $\mathbf{x} + r(\text{clip}(\bar{\mathbf{d}}_1 + \xi, -1, 1))$. This stochasticity sufficiently diversifies the query patterns, preventing the generation of identical fingerprints and thereby evading the collision-based detection mechanism. Adhering to the official settings for ImageNet, we use a detection threshold of 25 and a window size of 50. Any attack triggering this threshold is marked as a failure, and the query count before detection is recorded as 1stDQ. As shown in Table 7, this strategy is remarkably effective: our method yields a 0% Detection Rate (DetR). In sharp contrast, competing SOTA methods are rendered ineffective, triggering the defense with a 100% DetR (except BouT at 95%).

5.5 Generalization to Dense Prediction Tasks

To evaluate the generalization of DPAttack across diverse vision tasks, we evaluate its performance on object detection and segmentation against the runner-up, ADBA (detailed settings in App. N). As summarized in Table 8, our method demonstrates superior efficacy and efficiency in both tasks. Notably, in the segmentation task, Ours_{dyn} outperforms ADBA by over 31.5% in ASR. This significant margin validates that our frequency-based priors are highly effective even for complex dense prediction models. Appendix Table 11 shows that our method still sustains an ASR improvement of over 30% with a 1,000-query budget.

5.6 Ablation Study

In this section, we analyze the key components of DPAttack: the DDM initialization and the PDO search module. We also investigate the impact of block size w . Complementary studies on the individual

Table 4: The attack performance on ObjectNet (ViT-H-14-CLIPA-336) under $\ell_\infty = 0.05$ constraint.

Metrics	ASR										Avg.Q						Med.Q								
	HSJA	BouR	BouT	TtBA	HRayS	ADBA	Ours _{opt}	Ours _{dyn}	HSJA	BouR	BouT	TtBA	HRayS	ADBA	Ours _{opt}	Ours _{dyn}	HSJA	BouR	BouT	TtBA	HRayS	ADBA	Ours _{opt}	Ours _{dyn}	
MaxQ	0.0	0.0	<u>10.0</u>	0.0	0.0	0.0	<u>21.5</u>	0.0	-	-	6	-	-	-	5	-	-	5	-	-	-	-	5	-	
10	0.0	5.5	5.5	15.0	0.0	5.0	7.5	<u>37.0</u>	<u>39.5</u>	13	13	20	-	41	41	16	22	12	12	6	-	39	42	10	20
50	20.5	18.0	22.5	9.5	13.0	20.5	<u>44.5</u>	<u>50.0</u>	40	42	35	77	72	61	25	33	61	58	6	76	81	58	15	20	
100	23.5	23.0	22.0	38.0	49.5	65.5	<u>67.5</u>	95	91	72	207	178	156	98	92	102	98	88	190	157	118	34	28		
500	25.0	23.5	25.5	32.5	51.0	61.0	<u>77.0</u>	<u>78.5</u>	136	129	137	363	326	257	194	186	151	149	6	313	220	162	55	49	
1k	26.5	22.5	26.5	58.5	73.0	<u>82.5</u>	<u>88.5</u>	242	141	202	1,105	770	636	371	364	152	149	137	850	430	290	86	65		
3k	27.0	25.0	29.5	73.0	82.0	<u>88.0</u>	<u>92.5</u>	637	130	197	1,692	1,171	872	536	523	152	149	8	1,356	565	313	98	82		
6k	33.0	24.5	27.5	83.0	91.5	<u>95.5</u>	<u>98.5</u>	98.0	1,123	412	137	2,437	2,135	1,527	1,039	1,022	154	148	7	1,650	853	362	124	92	
15k	37.5	22.5	28.5	89.5	96.5	<u>99.0</u>	<u>99.5</u>	3,880	107	203	3,498	3,024	2,244	1,366	1,399	155	148	138	1,952	940	509	171	99		
30k	40.0	24.5	30.0	89.5	95.5	99.5	<u>100.0</u>	6,552	114	225	4,460	1,211	2,426	1,367	1,555	153	149	8	2,125	651	518	141	103		
40k																									

Table 5: The attack performance on real-world APIs under different perturbation constraints. Abbreviations: ASR: A., Med.Q: M.Q, Avg.Q: A.Q.

ℓ_∞	APIs	Imaggia			Google			Tencent			Baidu		
		A.	M.Q	A.Q	A.	M.Q	A.Q	A.	M.Q	A.Q	A.	M.Q	A.Q
0.05	ADBA	83	61	105	53	26	28	33	25	26	65	25	26
	Ours _{opt}	90	6	38	91	22	23	67	10	15	88	9	13
	Ours _{dyn}	100	23	20	100	21	19	75	23	20	90	21	20
0.1	ADBA	99	41	70	68	24	26	56	33	35	80	24	27
	Ours _{opt}	100	4	8	94	7	14	100	14	14	98	7	14
	Ours _{dyn}	100	16	16	100	15	16	97	17	16	99	16	16

Table 6: The attack performance on adversarially trained models under different perturbation constraints. The query limit is 1,000.

Dataset	Metrics	HSJA	BouR	BouT	TtBA	HRayS	ADBA	Ours _{opt}	Ours _{dyn}
CIFAR-10	ASR	4.5	3.5	3.5	1.5	20.5	20.0	<u>22.5</u>	<u>21.0</u>
	Avg.Q	140	141	58	361	290	211	234	205
	Med.Q	140	140	8	398	222	101	143	83
ImageNet	ASR	10.5	10.5	11.0	3.5	44.5	45.0	50.5	<u>48.5</u>
	Avg.Q	112	111	84	302	189	143	143	191
	Med.Q	149	146	6	223	91	58	73	90

Table 7: The attack performance on Blacklight. Except for our method, other methods yield the same results under both query limits of 100 and 500.

Methods	ASR	Avg.Q	Med.Q	DetR	1stDQ
HSJA	0	-	-	100	9
BouR	0	-	-	100	9
BouT	5	5	5	95	8
TtBA	0	-	-	100	11
HRayS	0	-	-	100	5
ADBA	0	-	-	100	2
Ours _{opt} (100)	33	41	36	0	-
Ours _{dyn} (100)	35	44	41	0	-
Ours _{opt} (500)	40	71	46	0	-
Ours _{dyn} (500)	44	93	59	0	-

Table 8: Comparison of attack performance on dense prediction tasks. The query limit is 50.

Methods	Object Detection			Segmentation		
	ASR	Avg.Q	Med.Q	ASR	Avg.Q	Med.Q
ADBA	17.0	30	29	4.5	36	35
Ours d_n	43.5	18	6	36.0	14	6
Ours _{opt}	35.5	16	10	<u>35.5</u>	17	10
Ours _{dyn}	<u>39.5</u>	22	20	33.5	20	18

Table 9: The ablation study on the initialization methods and PDO module. Abbreviation: WideResNet-50 (wrs50); all one vector (1); dyadic search used in ADBA (ADBA), see Step 2 of ADBA in Sec. 2.3.

Model	Search	Gauss.	Unif.	Img.	1	d_b	d_r	d_n	DDM
ViT	ADBA	52.5	62.5	76.5	75.5	63.5	75.5	75.5	77.0
	PDO	70.5	72.0	76	75.5	82.5	81.5	85.5	85.5
wrs50	ADBA	16.5	18.0	36.5	45.0	27.5	35.0	28.5	37.0
	PDO	42.0	43.5	43.0	45.0	44.0	48.0	47.0	50.5

contributions of $d_n/\phi(\hat{d}_r)$ in DDM and frequency sampling priors are detailed in App. D.

Effectiveness of DDM Initialization. To evaluate our DDM initialization, we compare it against standard baselines (Gaussian, Uniform, Random Images, and All-ones vector 1) while keeping the subsequent PDO search fixed. As shown in Table 9, DDM significantly outperforms traditional priors. For instance, on ViT, DDM achieves an ASR of 85.5%, outstripping Gaussian and Uniform initializations by 15.0% and 13.5%, respectively. On the robust WideResNet-50, DDM still provides a substantial gain (+8.5% over Gaussian). Notably, the slight advantage of DDM over individual components (d_b , d_r , d_n) highlights the necessity of our integrated initialization pipeline. These results confirm that DDM provides a *structurally informative prior* that aligns with the target model's spectral sensitivity, thereby boosting search efficiency.

Efficacy of PDO. The PDO module is designed to refine the initial direction. To assess its impact, we replace PDO with a basic structured dyadic search (denoted as ADBAS, the search strategy used in ADBA). Focusing on the last column in Table 9, we observe that under DDM initialization, PDO outperforms ADBAS by 8.5% on ViT and 13.5% on WideResNet-50. This empirically validates Theorems 4 and 5, proving that PDO's sign-consistent run partitioning is superior to fixed dyadic splitting. When initialized with an unstructured vector (1), the ASRs of PDO and ADBAS are identical (e.g., 45.0% on wrs50). This demonstrates that without an initial spatial structure, PDO correctly degrades to a standard dyadic search, whereas its true power is unlocked when paired with DDM's structural priors.

Influence of Block Size w . We evaluate the sensitivity of the block size $w \in \{4, 8, 16, 32\}$ on ImageNet (224 × 224). While the overall ASR remains relatively stable (as illustrated in Fig. 8), the optimal w for maximizing performance is highly architecture-dependent. For instance, WideResNet-50 reaches its peak ASR at $w = 16$, whereas ViT-B-32 performs best at $w = 4$. Furthermore, the choice of w

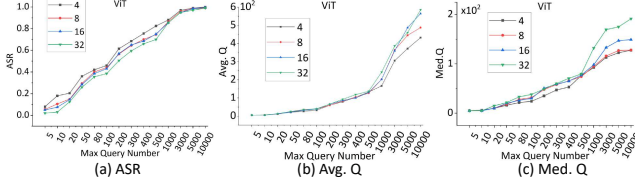


Figure 8: The influence of block size w used in BDCT.

leads to significant fluctuations in query efficiency, with the Avg.Q varying by over 100 as shown in Fig. 8. This “one-size-does-not-fit-all” observation underscores the necessity of our dynamic block size selection algorithm, which adaptively identifies a suitable w for a given target model to achieve better ASR and query efficiency.

6 Conclusion

In this work, we propose DPAttack, a highly efficient hard-label black-box attack framework that bridges spectral sensitivity with spatial structural search. By leveraging a systematic analysis of adversarial sensitivity across BDCT frequency coefficients, we develop a customized initialization strategy that provides a structurally informative starting point. To exploit this prior, we introduce a pattern-driven direction optimization module, which significantly accelerates gradient sign estimation by searching along sign-consistent runs. Furthermore, we establish a novel theoretical framework for hard-label sign-flipping attacks, providing proofs for the superiority of our initialization and search strategies. Extensive experiments across various architectures, datasets, tasks and real-world APIs demonstrate that DPAttack consistently surpasses SOTA methods in both attack success rate and query efficiency.

References

- [1] Abdullah Al-Dujaili and Una-May O'Reilly. 2020. Sign bits are all you need for black-box attacks. In *ICLR*.
- [2] Maksym Andriushchenko, Francesco Croce, Nicolas Flammarion, and Matthias Hein. 2020. Square attack: a query-efficient black-box adversarial attack via random search. In *ECCV*.
- [3] Apple. 2023. Apple Core ML. <https://developer.apple.com/cn/machine-learning/core-ml/>.
- [4] Baidu. 2024. Image Recognition. <https://cloud.baidu.com/doc/IMAGERECOGNITION/index.html>.
- [5] Andrei Barbu, David Mayo, Julian Alverio, William Luo, Christopher Wang, Dan Gutfreund, Josh Tenenbaum, and Boris Katz. 2019. Objectnet: A large-scale bias-controlled dataset for pushing the limits of object recognition models. In *NeurIPS*, Vol. 32.
- [6] Wieland Brendel, Jonas Rauber, and Matthias Bethge. 2018. Decision-Based Adversarial Attacks: Reliable Attacks Against Black-Box Machine Learning Models. In *ICLR*.
- [7] Jinghui Chen and Quanquan Gu. 2020. RayS: A Ray Searching Method for Hard-label Adversarial Attacks. In *KDD*.
- [8] Jianbo Chen, Michael I Jordan, and Martin J Wainwright. 2020. Hopskipjumpattack: A query-efficient decision-based attack. In *IEEE S&P*.
- [9] Yiting Chen, Qibing Ren, and Junchi Yan. 2022. Rethinking and improving robustness of convolutional neural networks: a shapley value-based approach in frequency domain. *NeurIPS* (2022).
- [10] Minhao Cheng, Thong Le, Pin-Yu Chen, Huan Zhang, JinFeng Yi, and Cho-Jui Hsieh. 2019. Query-Efficient Hard-label Black-box Attack: An Optimization-based Approach. In *ICLR*.
- [11] Minhao Cheng, Simranjit Singh, Patrick Chen, Pin Yu Chen, Sijia Liu, and Cho Jui Hsieh. 2020. SIGN-OPT: A QUERY-EFFICIENT HARD-LABEL ADVERSARIAL ATTACK. In *ICLR*.
- [12] Minhao Cheng, Huan Zhang, Cho-Jui Hsieh, Thong Le, Pin-Yu Chen, and Jinfeng Yi. 2019. Query-efficient hard-label black-box attack: An optimization-based approach. In *ICLR*.
- [13] Francesco Croce, Maksym Andriushchenko, Vikash Sehwag, Edoardo Debenedetti, Nicolas Flammarion, Mung Chiang, Prateek Mittal, and Matthias Hein. 2021. RobustBench: a standardized adversarial robustness benchmark. In *NeurIPS*.
- [14] Francesco Croce and Matthias Hein. 2020. Minimally Distorted Adversarial Examples with a Fast Adaptive Boundary Attack. In *ICML*.
- [15] Media Cybernetics. [n. d.]. Mediacy. <https://mediacy.com/>.
- [16] Jia Deng, Wei Dong, Richard Socher, Li-Jia Li, Kai Li, and Li Fei-Fei. 2009. Imagenet: A large-scale hierarchical image database. In *CVPR*. IEEE, 248–255.
- [17] Jiankang Deng, Jia Guo, Niannan Xue, and Stefanos Zafeiriou. 2019. Arcface: Additive angular margin loss for deep face recognition. In *Proceedings of the IEEE/CVF conference on computer vision and pattern recognition*. 4690–4699.
- [18] Y. Dong, F. Liao, T. Pang, H. Su, J. Zhu, X. Hu, and J. Li. 2018. Boosting Adversarial Attacks with Momentum. In *CVPR*.
- [19] Logan Engstrom, Andrew Ilyas, Hadi Salman, Shibani Santurkar, and Dimitris Tsipras. 2019. Robustness. <https://github.com/MadryLab/robustness>.
- [20] N Benjamin Erichson, Soon Ho Lim, Francisco Utrera, Winnie Xu, Ziang Cao, and Michael W Mahoney. 2024. Noisymix: Boosting robustness by combining data augmentations, stability training, and noise injections. In *AISTATS*.
- [21] Zheng Fang, Tao Wang, Lingchen Zhao, Shenyi Zhang, Bowen Li, Yunjie Ge, Qi Li, Chao Shen, and Qian Wang. 2024. Zero-query adversarial attack on black-box automatic speech recognition systems. In *ACM CCS*. 630–644.
- [22] Rafael C. Gonzalez and Richard E. Woods. 2018. *Digital Image Processing* (4th ed.). Pearson.
- [23] Google. [n. d.]. Google Cloud Vision API. <https://cloud.google.com/vision?hl=en>.
- [24] Chuan Guo, Jacob Gardner, Yurong You, Andrew Gordon Wilson, and Kilian Weinberger. 2019. Simple black-box adversarial attacks. In *ICLR*.
- [25] Chuan Guo, Mayank Rana, Moustapha Cisse, and Laurens van der Maaten. 2018. Countering Adversarial Images using Input Transformations. In *ICLR*.
- [26] Dan Hendrycks, Steven Basart, Norman Mu, Saurav Kadavath, Frank Wang, Evan Dorundo, Rahul Desai, Tyler Zhu, Samyak Parajuli, Mike Guo, et al. 2021. The many faces of robustness: A critical analysis of out-of-distribution generalization. In *ICCV*. 8340–8349.
- [27] Dan Hendrycks and Thomas Dietterich. 2019. Benchmarking Neural Network Robustness to Common Corruptions and Perturbations. In *ICLR*.
- [28] Christian Szegedy Ian J. Goodfellow, Jonathon Shlens. 2015. Explaining and Harnessing Adversarial Examples. In *ICLR*.
- [29] Gabriel Ilharco, Mitchell Wortsman, Ross Wightman, Cade Gordon, Nicholas Carlini, Rohan Taori, Achal Dave, Vaishaal Shankar, Hongseok Namkoong, John Miller, Hannaneh Hajishirzi, Ali Farhadi, and Ludwig Schmidt. 2021. *OpenCLIP*. doi:10.5281/zenodo.5143773 If you use this software, please cite it as below..
- [30] Andrew Ilyas, Logan Engstrom, and Aleksander Madry. 2019. Prior Convictions: Black-box Adversarial Attacks with Bandits and Priors. In *ICLR*.
- [31] Imaga. [n. d.]. AI-Powered Image Tagging API. <https://imgaga.com/solutions/auto-tagging>.
- [32] Shuaifan Jin, He Wang, Zhibo Wang, Feng Xiao, Jiahui Hu, Yuan He, Wenwen Zhang, Zhongjie Ba, Weijie Fang, Shuhong Yuan, et al. 2024. Defending Deep Learning-based Privacy Attacks with Gradient Descent-resistant Features in Face Recognition. In *USENIX*.
- [33] Alexander Kirillov, Eric Mintun, Nikhila Ravi, Hanzi Mao, Chloe Rolland, Laura Gustafson, Tete Xiao, Spencer Whitehead, Alexander C Berg, Wan-Yen Lo, et al. 2023. Segment anything. In *ICCV*. 4015–4026.
- [34] Alex Krizhevsky, Geoffrey Hinton, et al. 2009. Learning multiple layers of features from tiny images. (2009).
- [35] Fengpeng Li, Kemou Li, Haiwei Wu, Jinyu Tian, and Jiantao Zhou. 2024. DAT: Improving Adversarial Robustness via Generative Amplitude Mix-up in Frequency Domain. In *NeurIPS*. 127099–127128.
- [36] Fengpeng Li, Kemou Li, Haiwei Wu, Jinyu Tian, and Jiantao Zhou. 2025. Toward Robust Learning via Core Feature-Aware Adversarial Training. *IEEE TIFS* 20 (2025), 6236–6251.
- [37] Huiying Li, Shawn Shan, Emily Wenger, Jiajun Zhang, Haitao Zheng, and Ben Y Zhao. 2022. Blacklight: Scalable defense for neural networks against Query-Based Black-Box attacks. In *USENIX*.
- [38] Tsung-Yi Lin, Michael Maire, Serge Belongie, James Hays, Pietro Perona, Deva Ramanan, Piotr Dollár, and C Lawrence Zitnick. 2014. Microsoft coco: Common objects in context. In *ECCV*. Springer, 740–755.
- [39] Chen Ma, Xiangyu Guo, Li Chen, Jun-Hai Yong, and Yisen Wang. 2021. Finding optimal tangent points for reducing distortions of hard-label attacks. *NeurIPS* (2021).
- [40] Aleksander Madry, Aleksandar Makelov, Ludwig Schmidt, Dimitris Tsipras, and Adrian Vladu. 2018. Towards Deep Learning Models Resistant to Adversarial Attacks. In *ICLR*.
- [41] Thibault Maho, Teddy Furon, and Erwan Le Merrer. 2021. Surfree: a fast surrogate-free black-box attack. In *CVPR*.
- [42] Mehryar Mohri, Afshin Rostamizadeh, and Ameet Talwalkar. 2018. *Foundations of Machine Learning*.

[43] Seungyong Moon, Gaon An, and Hyun Oh Song. 2019. Parsimonious black-box adversarial attacks via efficient combinatorial optimization. In *ICLR*.

[44] Donald B. Owen. 1956. Tables for Computing Bivariate Normal Probabilities. *The Annals of Mathematical Statistics* 27, 4 (1956), 1075–1090. doi:10.1214/aoms/1177728074

[45] PyTorch. 2023. <https://github.com/pytorch/vision>.

[46] Alec Radford, Jong Wook Kim, Chris Hallacy, Aditya Ramesh, Gabriel Goh, Sandhini Agarwal, Girish Sastry, Amanda Askell, Pamela Mishkin, Jack Clark, et al. 2021. Learning transferable visual models from natural language supervision. In *ICLR*.

[47] S. Rosenbaum. 1961. Moments of a Truncated Bivariate Normal Distribution. *Journal of the Royal Statistical Society: Series B (Methodological)* 23, 2 (1961), 405–408. doi:10.1111/j.2517-6161.1961.tb00422.x

[48] Meng Shen, Changyue Li, Qi Li, Hao Lu, Liehuang Zhu, and Ke Xu. 2024. Transferability of white-box perturbations: query-efficient adversarial attacks against commercial DNN services. In *USENIX*.

[49] Tencent. 2024. Tencent General Image Label. “<https://cloud.tencent.com/document/product/865/75196>”.

[50] Florian Tramèr, Alexey Kurakin, Nicolas Papernot, Ian Goodfellow, Dan Boneh, and Patrick McDaniel. 2018. Ensemble Adversarial Training: Attacks and Defenses. In *ICLR*.

[51] J.H. Van Vleck and D. Middleton. 1966. The spectrum of clipped noise. *Proc. IEEE* 54, 1 (1966), 2–19.

[52] Viet Quoc Vo, Ehsan Abbasnejad, and Damith C Ranasinghe. 2022. RamBoAttack: A Robust Query Efficient Deep Neural Network Decision Exploit. In *NDSS*.

[53] Gregory K Wallace. 1991. The JPEG still picture compression standard. *Commun. ACM* 34, 4 (1991), 30–44.

[54] Jie Wan, Jianhao Fu, Lijin Wang, and Ziqi Yang. 2024. Bounceattack: A query-efficient decision-based adversarial attack by bouncing into the wild. In *IEEE S&P*.

[55] Feiyang Wang, Xingquan Zuo, Hai Huang, and Gang Chen. 2025. ADBA: Approximation Decision Boundary Approach for Black-Box Adversarial Attacks. *AAAI* (2025).

[56] Feiyang Wang, Xingquan Zuo, Hai Huang, and Gang Chen. 2025. TtBA: Two-third Bridge Approach for Decision-Based Adversarial Attack. In *ICML*.

[57] Binyan Xu, Xilin Dai, Di Tang, and Kehuan Zhang. 2025. One Surrogate to Fool Them All: Universal, Transferable, and Targeted Adversarial Attacks with CLIP. In *ACM CCS*. 3087–3101.

[58] Jiancheng Yang, Rui Shi, and Bingbing Ni. 2021. MedMNIST Classification Decathlon: A Lightweight AutoML Benchmark for Medical Image Analysis. In *ISBI*. 191–195.

[59] Jiancheng Yang, Rui Shi, Donglai Wei, Zequan Liu, Lin Zhao, Bilian Ke, Hanspeter Pfister, and Bingbing Ni. 2023. Medmnist v2-a large-scale lightweight benchmark for 2d and 3d biomedical image classification. *Scientific Data* 10, 1 (2023), 41.

[60] Jiancheng Yang, Rui Shi, Donglai Wei, Zequan Liu, Lin Zhao, Bilian Ke, Hanspeter Pfister, and Bingbing Ni. 2023. MedMNIST v2-A large-scale lightweight benchmark for 2D and 3D biomedical image classification. *Scientific Data* 10, 1 (2023), 41.

[61] Zhewei Yao, Amir Gholami, Kurt Keutzer, and Michael W Mahoney. 2020. Pyhessian: Neural networks through the lens of the hessian. In *2020 IEEE international conference on big data (Big data)*. IEEE, 581–590.

[62] Dong Yin, Raphael Gontijo Lopes, Jon Shlens, Ekin Dogus Cubuk, and Justin Gilmer. 2019. A fourier perspective on model robustness in computer vision. *NeurIPS* 32 (2019).

[63] H. Zhang, Y. Avirthis, T. Furon, and L. Amsaleg. 2021. Walking on the Edge: Fast, Low-Distortion Adversarial Examples. *IEEE TIFS* (2021).

[64] Baolin Zheng, Peipei Jiang, Qian Wang, Qi Li, Chao Shen, Cong Wang, Yunjie Ge, Qingyang Teng, and Shenyi Zhang. 2021. Black-box adversarial attacks on commercial speech platforms with minimal information. In *ACM CCS*. 86–107.

A Proof of Theorem 1

THEOREM 1 (APPROXIMATION LOWER BOUND FOR NRAYS).

Let $\mathbf{u} \in \mathbb{S}^{d-1}$ be an arbitrary unit vector. Let $\{\mathbf{d}_j\}_{j=1}^m$ be m vectors sampled independently and uniformly from the binary hypercube $\mathcal{H} \equiv \{-1, +1\}^d$, and let $\hat{\mathbf{d}}_j = \mathbf{d}_j / \sqrt{d}$ be their normalized counterparts. For any precision $\zeta \in (0, 1)$ and confidence $\delta \in (0, 1)$, there exists a constant $C \geq 1$ such that if the sample size satisfies $m \geq -(\ln \delta) e^{Cd\zeta^2}$, then with probability at least $1 - \delta$, there exists at least one index $j \in \{1, \dots, m\}$ satisfying:

$$\mathbf{u}^\top \hat{\mathbf{d}}_j \geq \zeta. \quad (23)$$

PROOF. For any unit vector $\mathbf{u} \in \mathbb{S}^{d-1}$, consider

$$X = \mathbf{u}^\top \hat{\mathbf{d}} = \frac{1}{\sqrt{d}} \sum_{i=1}^d \mathbf{u}[i] \mathbf{d}[i], \quad (24)$$

where $\mathbf{d}[i] \in \{\pm 1\}$ are independent Rademacher random variables [42] (i.e., uniformly sampled from $\{\pm 1\}$). Conditioned on the fixed vector \mathbf{u} , the randomness of X arises solely from the random signs $\mathbf{d}[i]$. Thus, X is a sum of independent, zero-mean random variables with respect to the randomness of \mathbf{d} . Define

$$X_i := \frac{\mathbf{u}[i] \mathbf{d}[i]}{\sqrt{d}}, \quad (25)$$

so that $X = \sum_{i=1}^d X_i$, where each X_i satisfies

$$X_i \in \left[-\frac{|\mathbf{u}[i]|}{\sqrt{d}}, \frac{|\mathbf{u}[i]|}{\sqrt{d}} \right].$$

After applying Hoeffding's inequality [42], $\forall t > 0$,

$$\begin{aligned} \mathbb{P}(X \geq \mathbb{E}[X] + t) &\leq \exp \left(-\frac{2t^2}{\sum_{i=1}^d (2|\mathbf{u}[i]|/\sqrt{d})^2} \right) \\ &\leq \exp \left(-\frac{t^2}{2\|\mathbf{u}\|_2^2} \cdot d \right). \end{aligned} \quad (26)$$

Since the variables $\mathbf{u}[i]$ and $\mathbf{d}[i]$ are independent and $\mathbb{E}[\mathbf{d}[i]] = 0$, we have:

$$\begin{aligned} \mathbb{E}[X] &= \sum_{i=1}^d \mathbb{E}[X_i] = \frac{1}{\sqrt{d}} \sum_{i=1}^d \mathbb{E}[\mathbf{u}[i] \mathbf{d}[i]] \\ &= \frac{1}{\sqrt{d}} \sum_{i=1}^d \mathbb{E}[\mathbf{u}[i]] \mathbb{E}[\mathbf{d}[i]] = 0. \end{aligned} \quad (27)$$

Therefore, in Eq. (26), by replacing $\mathbb{E}[X] = 0$, $\|\mathbf{u}\|_2^2 = 1$ and let t be a positive cosine similarity value $\zeta \in (0, 1)$, we obtain:

$$\mathbb{P}(X \geq \zeta) \leq \exp \left(-\frac{C\zeta^2 d}{2} \right). \quad (28)$$

We define the probability p of the event $X \geq \zeta$ occurs as:

$$p = \mathbb{P}(X \geq \zeta) := \exp \left(-\frac{C\zeta^2 d}{2} \right), \quad (29)$$

where the constant $C \geq 1$ that makes $\exp(-C\zeta^2 d/2) \leq \exp(-\zeta^2 d/2)$ and satisfies Eq. (28). We independently sample m vectors \mathbf{d}_j from \mathcal{H} , recalling $\hat{\mathbf{d}}_j = \mathbf{d}_j / \sqrt{d}$. Each $X_j := \mathbf{u}^\top \hat{\mathbf{d}}_j$ satisfies:

$$\mathbb{P}(X_j < \zeta) = 1 - p. \quad (30)$$

Then the probability of all m failures is $(1 - p)^m$. Since we have $-p \geq -1$, by applying Bernoulli's inequality, we have:

$$(1 - p)^m \leq \exp(-pm). \quad (31)$$

To ensure that the probability of all m samples failing is at most δ ($0 < \delta < 1$), it suffices to require

$$\exp(-pm) \leq \delta \Rightarrow m \geq -(\ln \delta) \exp(C\zeta^2 d). \quad (32)$$

Under this condition, the probability that at least one sampled direction $\mathbf{d}_j \in \{\pm 1\}^d$ satisfies $X_j \geq \zeta$ is at least $1 - \delta$, i.e.,

$$\mathbb{P}\left(\exists j \in \{1, \dots, m\} \text{ such that } \mathbf{u}^\top \hat{\mathbf{d}}_j \geq \zeta\right) \geq 1 - \delta. \quad (33)$$

Hence completes the proof. \square

B Proof of Theorem 2

ASSUMPTION 1. *We assume that the CE loss $\mathcal{L}(\mathbf{x}, y)$ is continuous and locally smooth [11, 12, 40] to ensure that first-order Taylor approximations of the loss are locally valid.*

ASSUMPTION 2. *The loss function $\mathcal{L}(\mathbf{x}, y) : \mathbb{R}^d \rightarrow \mathbb{R}$ satisfies subset-wise directional Lipschitz continuity with a constant $R > 0$. This means that for any vector $\mathbf{d} \in \mathcal{H}$, any subset $B_k^{(l)}$ (shortened as B), and the vector $\mathbf{d}_k^{(l)}$ (abbreviated as \mathbf{d}_B) obtained by flipping the signs of \mathbf{d} 's elements whose indices are within subset B , the following holds:*

$$|\mathcal{L}(\mathbf{x} + g(\mathbf{d}) \cdot \mathbf{d}_B) - \mathcal{L}(\mathbf{x} + g(\mathbf{d}) \cdot \mathbf{d})| \leq R \|\mathbf{d}_B - \mathbf{d}\|_1. \quad (34)$$

Remark. As gradients exhibit local similarity [30], Assumption 2 holds in most cases. We provide a more detailed discussion in Appendix C. Moreover, while the ℓ_2 norm is standard for Lipschitz analysis, in this specific scenario, the ℓ_1 norm offers a more straightforward and practically meaningful measure, especially when dealing with vectors with values in $\{\pm 1\}$ and subset operations. It allows the Lipschitz constant R to be more connected to the length of the flipped subset.

Assumption 2 guarantees that loss variations induced by subset-wise sign flips are well-controlled, while Assumption 1 ensures that first-order Taylor approximations of the loss are locally valid. Together, these regularity conditions allow observed loss differences to serve as reliable proxies for directional derivative influences, leading to the following subset selection guarantee. We now formalize this notion by introducing the following subset-wise influence measure.

DEFINITION 1 (SUBSET-WISE DIRECTIONAL DERIVATIVE INFLUENCE). *For a selected index subset $B_{ks}^{(l)}$ at round l of HRayS (following the definition in Step 2 of HRayS; see Sec. 2.3), we define its influence as the cumulative magnitude of the gradient components within that subset:*

$$I(B_{ks}^{(l)}) := \sum_{i \in B_{ks}^{(l)}} \left| \frac{\partial \mathcal{L}(\tilde{\mathbf{x}}, y)}{\partial \tilde{\mathbf{x}}[i]} \right|_{\tilde{\mathbf{x}}=\mathbf{x}+g(\mathbf{d}_{best})\mathbf{d}_{best}}. \quad (35)$$

This metric quantifies the collective contribution of the dimensions in $B_{ks}^{(l)}$ to the local increase of the loss. A larger $I(\cdot)$ implies the subset contains high-impact dimensions. Based on this influence measure, we establish the following subset selection guarantee for HRayS.

LEMMA 1. *Under Assumptions 1 and 2, the subset $B_{ks}^{(l)}$ selected by HRayS at round l satisfies:*

$$I(B_{ks}^{(l)}) \geq \max_{B_k^{(l)}} I(B_k^{(l)}) - \eta_l, \quad (36)$$

where η_l represents the selection error bound at round l .

PROOF. We prove Lemma 1 by relating the loss variation induced by a subset flip to its directional derivative influence.

Let $\tilde{\mathbf{x}} = \mathbf{x} + g(\mathbf{d})\mathbf{d}$ and $\Upsilon = g(\mathbf{d})(\mathbf{d}_B - \mathbf{d})$. By a first-order Taylor expansion of \mathcal{L} around $\tilde{\mathbf{x}}$, we have

$$\mathcal{L}(\tilde{\mathbf{x}} + \Upsilon) - \mathcal{L}(\tilde{\mathbf{x}}) = \nabla \mathcal{L}(\tilde{\mathbf{x}})^\top \Upsilon + o(\|\Upsilon\|). \quad (37)$$

Ignoring higher-order terms, this gives

$$\mathcal{L}(\tilde{\mathbf{x}} + \Upsilon) - \mathcal{L}(\tilde{\mathbf{x}}) \approx g(\mathbf{d}) \sum_{i \in B} \nabla \mathcal{L}(\tilde{\mathbf{x}})[i] (\mathbf{d}_B[i] - \mathbf{d}[i]). \quad (38)$$

Since $\mathbf{d}_B[i] = -\mathbf{d}[i]$ for all $i \in B$, we have $\mathbf{d}_B[i] - \mathbf{d}[i] = -2\mathbf{d}[i]$, and therefore

$$\mathcal{L}(\tilde{\mathbf{x}} + \Upsilon) - \mathcal{L}(\tilde{\mathbf{x}}) \approx -2g(\mathbf{d}) \sum_{i \in B} \nabla \mathcal{L}(\tilde{\mathbf{x}})[i] \mathbf{d}[i]. \quad (39)$$

Taking absolute values and applying the triangle inequality yields

$$|\mathcal{L}(\tilde{\mathbf{x}} + \Upsilon) - \mathcal{L}(\tilde{\mathbf{x}})| \leq 2g(\mathbf{d}) \sum_{i \in B} |\nabla \mathcal{L}(\tilde{\mathbf{x}})[i]| = 2g(\mathbf{d}) I(B). \quad (40)$$

On the other hand, by Assumption 2 (subset-wise Lipschitz continuity), we have

$$|\mathcal{L}(\tilde{\mathbf{x}} + \Upsilon) - \mathcal{L}(\tilde{\mathbf{x}})| \leq R \|\mathbf{d}_B - \mathbf{d}\|_1 = 2R|B|. \quad (41)$$

Equations (40) and (41) together imply that the loss variation induced by flipping a subset B is a bounded and monotone function of its directional derivative influence $I(B)$.

At round l , HRayS selects a subset $B_{ks}^{(l)}$ whose induced loss change is within η_l of the maximum achievable loss change over all candidate subsets $\{B_k^{(l)}\}$. Since the loss change is monotone in $I(B)$, this directly implies

$$I(B_{ks}^{(l)}) \geq \max_{B_k^{(l)}} I(B_k^{(l)}) - \eta_l, \quad (42)$$

which completes the proof. \square

Remark. Assumption 2 is not used to derive a tight bound on $I(B)$, but rather to ensure that loss variations induced by subset-wise sign flips are comparable across different subsets. This regularity justifies using empirical loss differences as a stable ranking criterion in HRayS's greedy subset selection.

Lemma 1 establishes that HRayS preserves high-influence gradient coordinates through greedy subset selection. To translate this influence-based property into a statement about the boundary distance function $g(\mathbf{d})$, we next relate $g(\mathbf{d})$ to the change in cross-entropy loss under local linearity.

At each round l , HRayS's behavior can be interpreted as evaluating whether a perturbation in a particular direction causes a significant decrease in $g(\mathbf{d}_{best})$ within a subspace (subset $B_{ks}^{(l)}$). Given the current best direction \mathbf{d}_{best} , we flip the coordinates in the subset $B_{ks}^{(l)}$ to obtain the direction $\mathbf{d}_{ks}^{(l)}$ (referring to Step 2 of HRayS in Sec. 2.3). We define:

$$\Delta_{B_{ks}^{(l)}} := g(\mathbf{d}_{best}) - g(\mathbf{d}_{ks}^{(l)}) \quad (43)$$

HRayS's strategy prioritizes greedily searching for the subsets $B_{ks}^{(l)}$ that maximize $\Delta_{B_k^{(l)}}$, and focuses finer-grained search in the next round. We next investigate the relationship between $g(\mathbf{d})$ and the loss function $\mathcal{L}(\mathbf{x} + g(\mathbf{d})\mathbf{d}, y)$, then combine this connection with Eq. (43) to derive the direction update mechanism of HRayS in relation to the CE loss.

LEMMA 2. *Under the assumption of a locally linear decision boundary, i.e., the classifier's logit function is $f(\mathbf{x}) = \mathbf{W}^\top \mathbf{x} + \mathbf{b}$, the boundary distance function $g(\mathbf{d})$ is approximately inversely proportional to the single-step change in softmax CE loss, $\Delta\mathcal{L} = \mathcal{L}(\mathbf{x} + g(\mathbf{d})\mathbf{d}, y) - \mathcal{L}(\mathbf{x}, y)$. That is:*

$$g(\mathbf{d}) \propto \frac{1}{\mathcal{L}(\mathbf{x} + g(\mathbf{d})\mathbf{d}, y) - \mathcal{L}(\mathbf{x}, y)} \quad (44)$$

PROOF. For any class $m \in \{1, \dots, M\}$, the logit value is $f_m(\mathbf{x})$. We assume \mathbf{x} with true class y is correctly classified and that the nearest class at the decision boundary is k where $k \neq y$. The linear decision boundary $\partial\mathcal{B}_{yk}$ between \mathbf{x} and the nearest class k is defined by the equation $f_y(\mathbf{x}) - f_k(\mathbf{x}) = 0$, which is:

$$(\mathbf{w}_y - \mathbf{w}_k)^\top \mathbf{x} + (b_y - b_k) = 0, \quad (45)$$

where \mathbf{w}_y represents the y -th column of the weight matrix \mathbf{W} . $g(\mathbf{d})$ is the distance from point \mathbf{x} along the direction vector \mathbf{d} to the decision boundary $\partial\mathcal{B}_{yk}$. The point $\mathbf{x} + g(\mathbf{d})\mathbf{d}$ lies on the boundary:

$$(\mathbf{w}_y - \mathbf{w}_k)^\top (\mathbf{x} + g(\mathbf{d})\mathbf{d}) + (b_y - b_k) = 0. \quad (46)$$

Derived from this, we obtain the formulation of $g(\mathbf{d})$ is:

$$\begin{aligned} g(\mathbf{d}) &= \frac{-((\mathbf{w}_y - \mathbf{w}_k)^\top \mathbf{x} + (b_y - b_k))}{(\mathbf{w}_y - \mathbf{w}_k)^\top \mathbf{d}} \\ &= \frac{-(f_y(\mathbf{x}) - f_k(\mathbf{x}))}{(\mathbf{w}_y - \mathbf{w}_k)^\top \mathbf{d}}. \end{aligned} \quad (47)$$

The intuition of this formula is: the distance to the boundary is proportional to the current logit margin and inversely proportional to the projection of direction \mathbf{d} onto the normal vector of the decision boundary $\mathbf{w}_y - \mathbf{w}_k$.

On the other hand, $\Delta\mathcal{L}$ is the change in the softmax CE loss after moving a small step α from \mathbf{x} along the direction \mathbf{d} . The softmax CE loss is defined as:

$$\mathcal{L}(\mathbf{x}, y) = -\log \frac{e^{f_y(\mathbf{x})}}{\sum_{m=1}^M e^{f_m(\mathbf{x})}} = -f_y(\mathbf{x}) + \log \sum_{m=1}^M e^{f_m(\mathbf{x})}. \quad (48)$$

For a small step size α , we can use a first-order Taylor expansion to approximate the change in the loss function:

$$\Delta\mathcal{L} = \mathcal{L}(\mathbf{x} + \alpha\mathbf{d}, y) - \mathcal{L}(\mathbf{x}, y) \approx \alpha \cdot \nabla \mathcal{L}(\mathbf{x}, y)^\top \mathbf{d}. \quad (49)$$

Now let's compute the gradient of the loss function $\nabla \mathcal{L}(\mathbf{x}, y)$ according to the chain rule.

$$\begin{aligned} \nabla \mathcal{L}(\mathbf{x}, y) &= \nabla_{\mathbf{x}} \left(-f_y(\mathbf{x}) + \log \sum_{m=1}^M e^{f_m(\mathbf{x})} \right) \\ &= -\mathbf{w}_y + \frac{\sum_{m=1}^M (e^{f_m(\mathbf{x})} \mathbf{w}_m)}{\sum_{m=1}^M e^{f_m(\mathbf{x})}} \\ &= \frac{\sum_{m=1}^M (e^{f_m(\mathbf{x})} (\mathbf{w}_m - \mathbf{w}_y))}{\sum_{m=1}^M e^{f_m(\mathbf{x})}}. \end{aligned} \quad (50)$$

Let $p_j(\mathbf{x}) = \frac{e^{f_j(\mathbf{x})}}{\sum_{m=1}^M e^{f_m(\mathbf{x})}}$ be the softmax probability for class j . We have:

$$\nabla \mathcal{L}(\mathbf{x}, y) = \sum_j p_j(\mathbf{x}) (\mathbf{w}_j - \mathbf{w}_y). \quad (51)$$

Substituting this gradient back into Eq. (49):

$$\Delta\mathcal{L} \approx \alpha \sum_j p_j(\mathbf{x}) (\mathbf{w}_j - \mathbf{w}_y)^\top \mathbf{d}. \quad (52)$$

To simplify the analysis, we make an assumption common in adversarial attack literature: when a point \mathbf{x} is near a decision boundary, its softmax probabilities are dominated by the two most relevant classes (the true class y and the nearest class k). Thus, $p_j(\mathbf{x}) \approx 0$ for $j \notin \{y, k\}$. Then,

$$\begin{aligned} \Delta\mathcal{L} &\approx \alpha (p_y(\mathbf{x}) (\mathbf{w}_y - \mathbf{w}_y)^\top \mathbf{d} + p_k(\mathbf{x}) (\mathbf{w}_k - \mathbf{w}_y)^\top \mathbf{d}) \\ &\approx \alpha p_k(\mathbf{x}) (\mathbf{w}_k - \mathbf{w}_y)^\top \mathbf{d}. \end{aligned} \quad (53)$$

By considering Eqs. (47) and (53) together, we obtain:

$$g(\mathbf{d}) \approx \frac{\alpha \cdot p_k(\mathbf{x}) (f_y(\mathbf{x}) - f_k(\mathbf{x}))}{\Delta\mathcal{L}}. \quad (54)$$

For a fixed point \mathbf{x} and a small step size α , the numerator is a positive constant that does not depend on the direction \mathbf{d} . Thus, we arrive at the final inverse proportionality:

$$g(\mathbf{d}) \propto \frac{1}{\Delta\mathcal{L}}. \quad (55)$$

□

Lemma 1 ensures that HRayS identifies subsets with near-maximal directional derivative influence, while Lemma 2 links this influence to loss variation and boundary proximity. Together, these results provide the analytical foundation for relating HRayS's hierarchical subset search to gradient-aligned direction recovery.

We now state an algorithmic assumption that characterizes the approximate greedy behavior of HRayS. This assumption is not required for the preceding analytical lemmas, but is essential for controlling error accumulation in the global guarantee of Theorem 2.

ASSUMPTION 3. *HRayS approximately selects subsets corresponding to steep ascent at the l -th round, i.e., the selection error η_l is bounded within a small range.*

THEOREM 2 (GRADIENT APPROXIMATION GUARANTEE FOR HRAYS). *Assume that the gradient magnitude is uniformly bounded, i.e., $\|\nabla \mathcal{L}(\mathbf{x}, y)\|_\infty \leq G_{\max}$. Let η_l denote the maximum deviation between the directional derivative influence of the subset $B_{ks}^{(l)}$ selected by HRayS at round l and that of the optimal subset $\arg \max_{B_k^{(l)}} I(B_k^{(l)})$. Let $\hat{\mathbf{d}}^*$ be the final direction produced by HRayS. Then, the alignment between $\hat{\mathbf{d}}^*$ and the true gradient sign satisfies*

$$\text{sgn}(\nabla \mathcal{L}(\mathbf{x}, y))^\top \hat{\mathbf{d}}^* \geq \frac{\|\nabla \mathcal{L}(\mathbf{x}, y)\|_1}{G_{\max}} \cdot (1 - \omega), \quad (56)$$

where $\omega = \sum_{l=1}^{\lceil \log_2 d \rceil} \eta_l \|\nabla \mathcal{L}(\mathbf{x}, y)\|_1^{-1}$ denotes the cumulative relative error induced by suboptimal subset selections across all hierarchical rounds.

PROOF. According to Eq. (43), for an invariant $g(\mathbf{d}_{best})$, maximizing $\Delta_{B_k^{(l)}}$ is approximately corresponds to minimize $g(\mathbf{d}_{ks}^{(l)})$ within all 2^l subsets. Based on Lemma 2, minimizing $g(\mathbf{d}_{ks}^{(l)})$ is approximately equivalent to maximizing $\mathcal{L}(\mathbf{x} + g(\mathbf{d}_{best})\mathbf{d}_{ks}^{(l)}) - \mathcal{L}(\mathbf{x} + g(\mathbf{d}_{best})\mathbf{d}_{best})$ within all 2^l subsets. Thus, Eq. (43) can be approximated as:

$$\Delta_{B_k^{(l)}} \propto \mathcal{L}(\mathbf{x} + g(\mathbf{d}_{best})\mathbf{d}_{ks}^{(l)}) - \mathcal{L}(\mathbf{x} + g(\mathbf{d}_{best})\mathbf{d}_{best}). \quad (57)$$

Consequently, when HRayS approximately greedily searches for the direction $\mathbf{d}_{ks}^{(l)}$ that maximizes the CE loss value $\mathcal{L}(\mathbf{x} + g(\mathbf{d}_{best})\mathbf{d}_{ks}^{(l)})$. This provides an intuitive explanation of Theorem 2. We now proceed with a formal proof of the theorem.

Recalling Definition 1 and Lemma 1, at each level l , HRayS retains the set of dimensions within each subset that exhibit the maximal sum of derivatives $I(B_{ks}^{(l)})$. This dimension set is progressively refined across rounds, ultimately yielding a selected coordinate set $S \subset \{1, \dots, d\}$ that tends to capture dimensions with large gradient magnitudes. Consequently, we can construct a ± 1 sign vector $\hat{\mathbf{d}}^*$ where each element

$$\hat{\mathbf{d}}^*[i] \approx \begin{cases} \text{sgn}\left(\frac{\partial \mathcal{L}(\mathbf{x}, y)}{\partial \mathbf{x}[i]}\right) & \text{if } i \in S, \\ 1 \text{ or } -1 & \text{otherwise,} \end{cases} \quad (58)$$

whose alignment with the true gradient's sign vector $\text{sgn}\nabla\mathcal{L}(\mathbf{x}, y)$ (shortened as $\text{sgn}\nabla\mathcal{L}(\mathbf{x})$) can be measured by their inner product. This inner product can be expanded as follows:

$$\text{sgn}\nabla\mathcal{L}(\mathbf{x})^\top \hat{\mathbf{d}}^* = \sum_{i \in S} \left| \text{sgn}\left(\frac{\partial \mathcal{L}(\mathbf{x})}{\partial \mathbf{x}[i]}\right) \right| + \sum_{i \notin S} \left| \text{sgn}\left(\frac{\partial \mathcal{L}(\mathbf{x})}{\partial \mathbf{x}[i]}\right) \right| \quad (59)$$

Taking expectation over the randomness of the unselected coordinates, the second term vanishes. Recalling Eqs. (7) and (36), we have

$$\begin{aligned} \text{sgn}(\nabla\mathcal{L}(\mathbf{x}, y))^\top \hat{\mathbf{d}}^* &= \sum_{i \in S} 1 \\ &\geq \frac{1}{G_{\max}} \sum_{i \in S} \left| \frac{\partial \mathcal{L}(\mathbf{x}, y)}{\partial \mathbf{x}[i]} \right| \\ &\geq \frac{1}{G_{\max}} \left(\|\nabla\mathcal{L}(\mathbf{x}, y)\|_1 - \sum_{l=1}^{\lceil \log_2 d \rceil} \eta_l \right). \end{aligned} \quad (60)$$

Rearranging the right-hand side of this inequality yields the following expression:

$$\text{sgn}(\nabla\mathcal{L}(\mathbf{x}, y))^\top \hat{\mathbf{d}}^* \geq \frac{\|\nabla\mathcal{L}(\mathbf{x}, y)\|_1}{G_{\max}} \cdot (1 - \varpi), \quad (61)$$

where $\varpi = \sum_{l=1}^{\lceil \log_2 d \rceil} \eta_l \|\nabla\mathcal{L}(\mathbf{x}, y)\|_1^{-1}$. Hence completes the proof. \square

C Discussion on Assumption 2

In this section, we justify Assumption 2 by leveraging the local similarity of gradient components. For vectors with $\{\pm 1\}$ entries, we have $\|\mathbf{d}_B - \mathbf{d}\|_1 = 2|B|$, where $|B|$ denotes the cardinality of subset B . Therefore, Eq. (34) can be rewritten as:

$$|\mathcal{L}(\mathbf{x} + g(\mathbf{d})\mathbf{d}_B) - \mathcal{L}(\mathbf{x} + g(\mathbf{d})\mathbf{d})| \leq 2R|B|. \quad (62)$$

Table 10: The ablation study on \mathbf{d}_n , $\phi(\hat{\mathbf{d}}_r)$ and PDO. Ours_{opt} serves as the baseline ASR; Increased: green background; Decreased: gray background.

Datasets	ImageNet (ViT-B-32)				CIFAR-10 (VGG-16-BN)				
	MaxQ	Ours _{opt}	w/ \mathbf{d}_n	w/ $\phi(\hat{\mathbf{d}}_r)$	w/o P.	MaxQ	Ours _{opt}	w/ \mathbf{d}_n	w/ $\phi(\hat{\mathbf{d}}_r)$
5	8.0	0.0	0.5	0.0	5	4.0	0.0	-4.0	0.0
10	18.5	0.0	-4.5	0.0	10	14.5	0.0	-10.5	0.0
50	30.0	-0.5	-5.0	-0.5	50	30.0	-2.5	-13.0	-4.5
80	41.5	-0.5	-6.0	-2.5	80	45.5	-3.5	-14.0	-1.5
100	44.5	4.0	-4.5	0.0	100	49.5	0.0	-12.5	2.5
200	64.5	4.0	-5.5	-6.5	150	62.0	-2.0	-13.0	0.0
300	74.5	1.5	-5.0	-11.0	200	76.0	-3.0	-16.0	-4.0
400	82.0	-1.0	-6.0	-10.0	250	80.0	-1.5	-13.0	-2.5
500	85.5	0.0	-7.5	-8.5	300	82.5	-0.5	-7.0	-1.5
1k	89.5	3.0	0.0	-5.0	400	87.5	-1.0	-7.0	1.0
3k	98.0	0.0	-1.0	-3.5	500	92.5	-3.5	-8.0	-3.0
5k	99.5	0.0	-0.5	-2.5	1k	98.5	-2.5	-5.0	-2.5
10k	100.0	0.0	-0.5	-0.5	2k	100.0	-1.5	-1.0	-1.5

Since $g(\mathbf{d})$ is fixed once \mathbf{d} is determined, we set $g(\mathbf{d}) = 1$ for notational simplicity. We assume that the gradient $\nabla\mathcal{L}(\mathbf{x}, y)$ exhibits *local similarity*, meaning that there exists a constant $\gamma > 0$ such that for any subset B consisting of consecutive indices,

$$\left| \frac{\partial \mathcal{L}(\tilde{\mathbf{x}}, y)}{\partial \tilde{\mathbf{x}}[i]} - \frac{\partial \mathcal{L}(\tilde{\mathbf{x}}, y)}{\partial \tilde{\mathbf{x}}[j]} \right| \leq \gamma, \quad \forall i, j \in B, \quad (63)$$

where $\tilde{\mathbf{x}} = \mathbf{x} + \mathbf{d}$. Let

$$s := \frac{1}{|B|} \sum_{i \in B} \left| \frac{\partial \mathcal{L}(\tilde{\mathbf{x}}, y)}{\partial \tilde{\mathbf{x}}[i]} \right| \Big|_{\tilde{\mathbf{x}}=\mathbf{x}+\mathbf{d}} \quad (64)$$

denote the average gradient value over subset B . By Eq. (63), each gradient component in B satisfies

$$\left| \frac{\partial \mathcal{L}(\tilde{\mathbf{x}}, y)}{\partial \tilde{\mathbf{x}}[i]} \right| \leq |s| + \gamma, \quad \forall i \in B. \quad (65)$$

Using the first-order Taylor expansion,

$$\mathcal{L}(\mathbf{x} + \mathbf{d}_B) - \mathcal{L}(\mathbf{x} + \mathbf{d}) \approx (\nabla\mathcal{L}(\tilde{\mathbf{x}}, y))^\top (\mathbf{d}_B - \mathbf{d}), \quad (66)$$

and noting that $\mathbf{d}_B[i] - \mathbf{d}[i] = -2d[i]$ for $i \in B$, we obtain

$$|\mathcal{L}(\mathbf{x} + \mathbf{d}_B) - \mathcal{L}(\mathbf{x} + \mathbf{d})| \leq 2 \sum_{i \in B} \left| \frac{\partial \mathcal{L}(\tilde{\mathbf{x}}, y)}{\partial \tilde{\mathbf{x}}[i]} \right|. \quad (67)$$

Applying Eq. (65) yields

$$|\mathcal{L}(\mathbf{x} + \mathbf{d}_B) - \mathcal{L}(\mathbf{x} + \mathbf{d})| \leq 2(|s| + \gamma)|B|. \quad (68)$$

Defining $R := |s| + \gamma$ completes the justification of Assumption 2.

D Additional Ablation Studies

D.1 Effect of Frequency Sampling Priors

To validate the robustness of our universal frequency-variance curve, we compare it against two model-specific strategies: (1) **Peak-Only Strategy**, which perturbs only the single optimal DCT channel (the peak of the BFS curve) for the target model; and (2) **Model-Tailored Strategy**, which employs the exact, model-specific BFS curve to generate the perturbation direction \mathbf{d}_n (see generation procedures in Sec. 4.3.2). Results indicate a clear trade-off between specificity and transferability. While the Peak-Only strategy boosts ASR on its matched model (e.g., ResNet-50: +8.5% / +5% at Max.Q=50/500), it suffers a severe performance drop on unmatched architectures (e.g., ViT: -21% drop). Similarly, the Model-Tailored

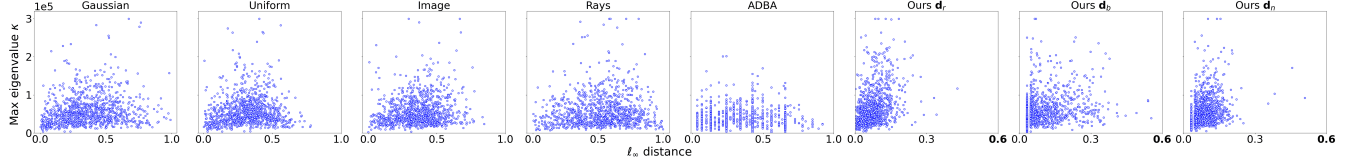


Figure 9: The relationship between boundary distance (ℓ_∞) and curvature κ across different initializations.

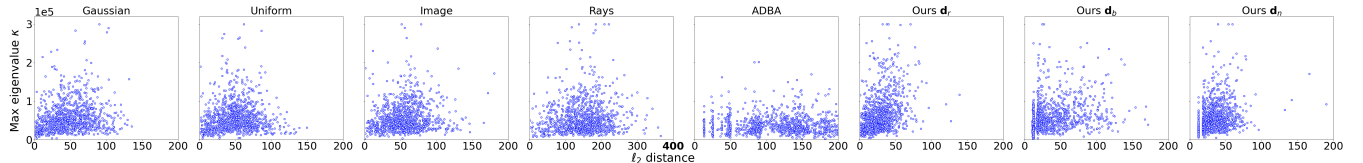


Figure 10: The relationship between boundary distance (ℓ_2) and curvature κ across different initializations.

strategy degrades performance on unseen models (ViT: $-8\%/-5\%$). This confirms that our balanced strategy effectively mitigates the risk of overfitting to specific spectral signatures, ensuring robust performance across diverse, unknown architectures.

D.2 The contribution of Directions d_n and d_a in the DDM

To further clarify the individual contributions of d_n and $d_a = \phi(\hat{d}_r)$ —both designed to improve initial direction—we introduce two new attack variants that apply only one of them during initialization, keeping all other settings unchanged. These variants, denoted as w/ d_n and w/ d_a , are evaluated in terms of ASR, as shown in Table 10. We perform the ablation study using Ours_{opt} (i.e. fixed optimal block size) as a representative example. Query counts are omitted due to their comparable performance. We can observe that, using only d_n without d_a even leads to an improvement in ASR for the ViT-B-32. This may be attributed to the high compatibility between the frequency-domain sensitivity of the ViT architecture and the frequency-based sampling strategy of d_n . In contrast, for lower-resolution datasets such as CIFAR-10, incorporating d_a is crucial for improving the ASR. But when using only d_a without d_n , the ASR generally degrades across models. These observations indicate that d_n plays a critical role in enhancing the overall ASR, while d_a which focuses on low-frequency components, serves to balance performance across diverse black-box models, without substantially compromising the ASR on models where d_n alone already performs well.

E Initialization of Direction d_r

The process for initializing d_r is formalized as follows: let the image height and width be H and W , the side length of color squares be h . The image with randomly colored squares can be formally represented as:

$$\mathbf{x}'_r = (\mathbf{a}_{ij})_{i=1, j=1}^{H, W} \quad \text{where} \quad \mathbf{a}_{i,j} = \mathbf{c}_{\lfloor i/h \rfloor, \lfloor j/h \rfloor}. \quad (69)$$

Spatial blocking is achieved through $\lfloor i/h \rfloor$ and $\lfloor j/h \rfloor$. The color square matrix \mathbf{c} is defined as:

$$\mathbf{c} \in \mathbb{Z}^{K \times L \times 3} \quad (K = \lceil H/h \rceil, L = \lceil W/h \rceil). \quad (70)$$

Each element $\mathbf{c}_{k,l}(R_{k,l}, G_{k,l}, B_{k,l})$ represents the RGB values of the block at position (k, l) . Color components satisfy

$$\begin{aligned} R_{k,l}, G_{k,l}, B_{k,l} &\in \{0, 1, \dots, 255\} \\ \text{with } \forall k, l : C_{k,l} &\sim U(\{0, 1, \dots, 255\}^3). \end{aligned} \quad (71)$$

Afterwards, we can obtain an image with randomly colored squares by performing the pixel mapping rule as follows:

$$\mathbf{a}_{i,j} = \begin{cases} \mathbf{c}_{k,l}, & x \in [kh + 1, (k + 1)h] \\ & \wedge y \in [lh + 1, (l + 1)h] \\ \text{Boundary}, & \text{otherwise} \end{cases} \quad (72)$$

When H and W are not integer multiples of h , boundary handling is performed via replication padding.

F Analysis on Direction Initialization Methods

We present the scatter plots comparing the ℓ_∞ or ℓ_2 perturbation distances and curvature variations of start points generated by different methods (as shown in Figs. 9 and 10). As observed, our proposed initialization directions d_r and d_n exhibit the tightest clustering towards the left side of the plot, while other methods show more dispersed and larger distances. This demonstrates that our d_r and d_n initialization directions can identify start points with greater local curvature under smaller adversarial perturbations. More examples of start points generated by different kinds of perturbation direction initialization methods are given in Fig. 11.

G Proof of Theorem 3

G.1 Setup and Notation

Let $U \in \mathbb{R}^{d \times d}$ denote the orthonormal BDCT basis ($U^\top U = I$), and let the BDCT coefficients be partitioned into C frequency channels. Let P_c denote the orthogonal projector onto the subspace corresponding to channel c . Let the initialization direction be generated as $\mathbf{x}_0 = U\mathbf{z}$, where $\mathbf{z} \in \mathbb{R}^d$ is a zero-mean Gaussian vector whose covariance is block-diagonal across frequency channels: $\mathbf{z} \sim \mathcal{N}(0, \Sigma_v)$, $\Sigma_v = \sum_{c=1}^C v_c P_c$. Equivalently, the components of \mathbf{z} restricted to each channel c are independently sampled as $\mathbf{z}|_c \sim \mathcal{N}(0, v_c I)$. Similarly, we introduce an auxiliary random vector in the BDCT domain, $\tilde{\mathbf{h}} \in \mathbb{R}^d$, which will later be endowed with specific statistical and



Figure 11: The illustration of AEs (dubbed start point) along different initial directions under ℓ_∞ constraint.

semantic interpretations. Let $\mathbf{h} = U\tilde{\mathbf{h}}$, where $\tilde{\mathbf{h}} \sim \mathcal{N}(0, \Sigma_s)$ with $\Sigma_s = \sum_{c=1}^C s_c P_c$.

Let $\mathbf{g} = \nabla_{\mathbf{x}} \mathcal{L}(\mathbf{x}, y) \in \mathbb{R}^d$ be the true gradient in the pixel space, and $\mathbf{u} = \text{sgn}(\mathbf{g}) \in \{-1, 1\}^d$ be its sign vector.

G.2 Assumptions and Lemmas

First, we present Lemma 3 to provide a quantitative link between the Pearson correlation of two Gaussian variables and the expected alignment of their sign vectors. This result will serve as the key analytical tool for translating second-order (covariance-level) alignment into first-order (sign-level) alignment in Theorem 3.

LEMMA 3 (ARCSINE LAW FOR GAUSSIAN SIGNS [51]). *Let (X, Y) be a pair of zero-mean jointly Gaussian random variables with correlation coefficient $\rho = \text{Corr}(X, Y) \in (-1, 1)$. Then:*

$$\mathbb{E}[\text{sgn}(X) \text{sgn}(Y)] = \frac{2}{\pi} \arcsin(\rho). \quad (73)$$

By extension, for jointly Gaussian vectors $\mathbf{X}, \mathbf{Y} \in \mathbb{R}^d$ with coordinate-wise correlations $\rho_i = \text{Corr}(X_i, Y_i)$, the expected normalized inner product of their signs is:

$$\frac{1}{d} \mathbb{E}[\langle \text{sgn}(\mathbf{X}), \text{sgn}(\mathbf{Y}) \rangle] = \frac{1}{d} \sum_{i=1}^d \frac{2}{\pi} \arcsin(\rho_i). \quad (74)$$

PROOF. Using the identity $\text{sgn}(t) = 2\mathbb{I}(t > 0) - 1$, we have:

$$\mathbb{E}[\text{sgn}(X)\text{sgn}(Y)] = 4\mathbb{P}(X > 0, Y > 0) - 1. \quad (75)$$

For bivariate normal variables, Sheppard's formula [44, 47] states that the orthant probability is $\mathbb{P}(X > 0, Y > 0) = \frac{1}{4} + \frac{1}{2\pi} \arcsin(\rho)$. Substituting this back yields the result. Linearity of expectation extends this to the vector case. \square

To analyze the expected alignment induced by the proposed initialization, we introduce a probabilistic model in the frequency domain. The following assumption specifies the joint second-order structure of the initialization and a surrogate gradient signal.

ASSUMPTION 4 (FREQUENCY-VARIANCE PRIOR WITH AVERAGE CHANNEL CORRELATION). *We assume that, for each channel c , the corresponding components of \mathbf{z} and $\tilde{\mathbf{h}}$ admit a Pearson correlation coefficient $\rho_c \in [-1, 1]$. While ρ_c may vary in sign across channels, we assume a weak aggregate bias:*

$$\mathbb{E}_c[\rho_c] > 0.$$

Under the probabilistic model introduced in Assumption 4, the following lemma characterizes how channel-wise correlations in the BDCT domain are transferred to pixel-wise correlations.

LEMMA 4 (CORRELATION TRANSFER). *For any pixel coordinate i , the Pearson correlation between $(\mathbf{x}_0)_i$ and $(\mathbf{h})_i$ is given by*

$$\rho_i = \frac{\sum_{c=1}^C \beta_{i,c} \rho_c \sqrt{v_c s_c}}{\sqrt{\sum_{c=1}^C \beta_{i,c} v_c} \sqrt{\sum_{c=1}^C \beta_{i,c} s_c}}, \quad (76)$$

where $\beta_{i,c} := \|(U^\top \mathbf{e}_i)_{|c}\|_2^2$ denotes the energy contribution of frequency channel c to pixel i .

PROOF. Both $(\mathbf{x}_0)_i$ and $(\mathbf{h})_i$ are zero-mean Gaussian random variables, as linear transformations of jointly Gaussian vectors. Their covariance is

$$\text{Cov}((\mathbf{x}_0)_i, (\mathbf{h})_i) = \sum_{c=1}^C \sum_{k \in \mathcal{I}_c} U_{ik}^2 \text{Cov}(z_k, \tilde{h}_k).$$

By assumption, for $k \in \mathcal{I}_c$, $\text{Cov}(z_k, \tilde{h}_k) = \rho_c \sqrt{v_c s_c}$, which yields

$$\text{Cov}((\mathbf{x}_0)_i, (\mathbf{h})_i) = \sum_{c=1}^C \beta_{i,c} \rho_c \sqrt{v_c s_c}.$$

The variances satisfy

$$\text{Var}((\mathbf{x}_0)_i) = \sum_{c=1}^C \beta_{i,c} v_c, \quad \text{Var}((\mathbf{h})_i) = \sum_{c=1}^C \beta_{i,c} s_c.$$

Normalizing the covariance by the standard deviations gives the stated expression. \square

The previous lemma establishes correlation transfer between the initialization and an auxiliary Gaussian vector. To relate this auxiliary variable \mathbf{h} to the true gradient of the loss $\nabla_{\mathbf{x}} \mathcal{L}$, we introduce the following modeling assumption.

ASSUMPTION 5 (CHANNEL-SENSITIVITY SURROGATE). *Let the variance s_c used for sampling \mathbf{h} is obtained by our BFS analysis method, we assume that this \mathbf{h} serves as a surrogate of the true gradient $\mathbf{g} = \nabla_{\mathbf{x}} \mathcal{L}$, in the sense that their sign vectors admit positive expected alignment:*

$$\frac{1}{d} \mathbb{E}[\langle \text{sgn}(\mathbf{h}), \text{sgn}(\mathbf{g}) \rangle] \geq 0.$$

Accordingly, we denote $\mathbf{g}^\# := \mathbf{h}$.

Justification of Assumption 5. We provide a justification showing that the surrogate vector $\mathbf{g}^\#$ constructed via BFS induces non-negative expected sign alignment with the true gradient \mathbf{g} .

Step 1: BFS as a monotone proxy for channel-wise gradient energy. For a frequency channel c , BFS evaluates

$$\text{BFS}_c = \mathbb{E}_{\delta_c} [\mathcal{L}(\mathbf{x} + \delta_c, y)],$$

where δ_c is a zero-mean random perturbation supported on channel c . By first-order Taylor expansion,

$$\mathcal{L}(\mathbf{x} + \delta_c, y) = \mathcal{L}(\mathbf{x}, y) + \langle \nabla_{\mathbf{x}} \mathcal{L}, \delta_c \rangle + o(\|\delta_c\|).$$

While the linear term vanishes in expectation, the magnitude of loss variation induced by δ_c is governed by the projected gradient energy $\|(U^\top \mathbf{g})_{|c}\|_2$. Consequently, BFS_c serves as a monotone proxy (up to a constant offset) for the channel-wise gradient energy in expectation.

Step 2: Construction of an energy-aligned Gaussian surrogate. Let $\mathbf{s} = (s_c)$ be defined proportional to BFS_c and construct $\tilde{\mathbf{g}} \sim \mathcal{N}(0, \Sigma_s)$ with $\Sigma_s = \sum_c s_c P_c$. Define the surrogate gradient $\mathbf{g}^\# = U\tilde{\mathbf{g}}$. By construction, channels with larger true gradient energy $\|(U^\top \mathbf{g})_{|c}\|_2^2$ are assigned larger variance s_c in the surrogate, implying second-order alignment between $\mathbf{g}^\#$ and \mathbf{g} in the BDCT domain.

Step 3: From second-order alignment to expected sign alignment. Each pixel coordinate aggregates contributions from multiple frequency channels under the orthonormal BDCT basis. As a result, the pixel-wise covariance $\text{Cov}((\mathbf{g}^\#)_i, \mathbf{g}_i)$ is a non-negative weighted sum of channel-wise energy alignments. This induces a non-negative average Pearson correlation:

$$\mathbb{E}_i[\text{Corr}((\mathbf{g}^\#)_i, \mathbf{g}_i)] \geq 0.$$

For jointly Gaussian variables, the Arcsine Law implies that expected sign agreement is a monotone function of the Pearson correlation. Applying this coordinate-wise yields

$$\frac{1}{d} \mathbb{E}[\langle \text{sgn}(\mathbf{g}^\#), \text{sgn}(\mathbf{g}) \rangle] \geq 0,$$

which establishes Assumption 5.

G.3 Proof of Theorem 3

Combining the correlation transfer property (Lemma 4), the sign-correlation relationship for Gaussian variables (Lemma 3), and the surrogate-gradient alignment assumption (Assumption 5), we establish a strictly positive expected alignment between the proposed initialization and the true gradient.

THEOREM 3 (POSITIVE EXPECTED ALIGNMENT UNDER FREQUENCY-VARIANCE PRIOR). *Let $\mathbf{x}_0 = U\mathbf{z}$ be the initialization generated under Assumption 4 with sign vector $\mathbf{d}_n = \text{sgn}(\mathbf{x}_0)$, and let \mathbf{h} be the proxy of the gradient under Assumption 4, $\mathbf{u} = \text{sgn}(\nabla_{\mathbf{x}} \mathcal{L})$ denote the sign of the true gradient. Under Lemma 4 and Assumption 5, the channel-wise correlations between \mathbf{x}_0 and \mathbf{h} induce coordinate-wise correlations between \mathbf{x}_0 and \mathbf{u} . Then the expected cosine alignment satisfies*

$$\frac{1}{d} \mathbb{E}[\langle \mathbf{d}_n, \mathbf{u} \rangle] = \frac{1}{d} \sum_{i=1}^d \mathbb{E}\left[\frac{2}{\pi} \arcsin(\rho_i)\right] > 0, \quad (77)$$

where $\rho_i = \text{Corr}((\mathbf{x}_0)_i, (\mathbf{h})_i)$ is given in Lemma 4. In contrast, for isotropic random initializations \mathbf{d}_{rand} , we have

$$\mathbb{E}[\langle \mathbf{d}_{\text{rand}}, \mathbf{u} \rangle] = 0.$$

PROOF. We now leverage the above preliminaries to prove Theorem 3. **1. Expected Alignment of \mathbf{d}_n .** Let $\mathbf{x}_0 = U\mathbf{z}$ be the pre-sign

initialization and $\mathbf{g}^\# = U\tilde{\mathbf{g}}$ be the gradient proxy defined under Assumptions 4 and 5. For each pixel coordinate i , denote

$$\rho_i := \text{Corr}((\mathbf{x}_0)_i, (\mathbf{g}^\#)_i),$$

which admits the explicit form given in Lemma 4.

Importantly, ρ_i is not required to be strictly positive for every i . However, under Assumption 4, the channel-wise correlations $\{\rho_c\}$ have a positive expectation, which induces a positive bias in the pixel-level correlations when aggregated across coordinates. As a result, aggregating across pixel coordinates yields a positive bias in expectation, namely,

$$\frac{1}{d} \sum_{i=1}^d \mathbb{E}[\rho_i] > 0.$$

Applying the Arcsine Law (Lemma 3) coordinate-wise and using the linearity of expectation, the expected sign alignment between $\mathbf{d}_n = \text{sgn}(\mathbf{x}_0)$ and $\mathbf{u}^\# = \text{sgn}(\mathbf{g}^\#)$ satisfies

$$\frac{1}{d} \mathbb{E}[\langle \mathbf{d}_n, \mathbf{u}^\# \rangle] = \frac{1}{d} \sum_{i=1}^d \mathbb{E}\left[\frac{2}{\pi} \arcsin(\rho_i)\right] > 0, \quad (78)$$

where the inequality follows from the monotonicity of $\arcsin(\cdot)$ on $(-1, 1)$ and the positive average correlation.

By Assumption 5, $\mathbf{u}^\#$ serves as a valid proxy for the true gradient sign \mathbf{u} in expectation, implying that the positive expected alignment transfers from $\mathbf{u}^\#$ to \mathbf{u} .

2. Comparison with Random Baselines. We now consider several common random initialization strategies \mathbf{d}_{rand} that are independent of \mathbf{u} :

- **Isotropic Noise (Gaussian or Uniform):** Let $\mathbf{d}_{\text{rand}} = \text{sgn}(\mathbf{z})$ with $\mathbf{z} \sim \mathcal{N}(0, I)$ or $\mathbf{z} \sim \mathcal{U}(-1, 1)^d$. By symmetry and independence, each coordinate agrees with \mathbf{u} with probability $1/2$, yielding $\mathbb{E}[\langle \mathbf{d}_{\text{rand}}, \mathbf{u} \rangle] = 0$.
- **Constant Directions:** For $\mathbf{d}_{\text{rand}} = \pm 1$, the expected alignment $\mathbb{E}[\sum_i u_i]$ vanishes under mild symmetry assumptions on the gradient. This symmetry is empirically substantiated by the zero-mean profile observed in Fig. 12, rendering the alignment negligible in practice.
- **Unrelated Clean Images:** When \mathbf{d}_{rand} is derived from an unrelated clean image, any residual correlation with \mathbf{u} is bounded by a small constant $\varepsilon_{\text{img}} \approx 0$ and lacks the systematic frequency alignment induced by Assumption 4.

Therefore, the proposed initialization \mathbf{d}_n achieves a strictly positive expected alignment with the true gradient, whereas standard random baselines yield zero expected alignment in expectation. This completes the proof. \square

COROLLARY 1 (BOUNDARY DISTANCE REDUCTION). *Under a local linear decision boundary model, the distance to the boundary $r(\mathbf{d})$ along direction \mathbf{d} is monotonically decreasing with the gradient alignment $\langle \mathbf{d}, \mathbf{u} \rangle$. Consequently, Theorem 3 implies that our initialization \mathbf{d}_0 yields a strictly smaller expected initial distance compared to random baselines.*

PROOF. We consider a local linear approximation of the decision boundary near the clean input \mathbf{x} . Let the decision boundary be

represented by the hyperplane:

$$\mathcal{B} = \{z \in \mathbb{R}^d \mid w^T z + b = 0\}, \quad (79)$$

where w is the normal vector to the boundary (parallel to the true gradient $\nabla_x \mathcal{L}$) and b is the bias. The normalized gradient direction is $u = w/\|w\|_2$.

Let R be the orthogonal (shortest) distance from x to the boundary \mathcal{B} . For any search direction d (where $\|d\|_2 = 1$), the distance $r(d)$ required to reach the boundary along d is determined by the intersection:

$$w^T(x + r(d)d) + b = 0. \quad (80)$$

Solving for $r(d)$, and noting that the orthogonal distance is $R = |w^T x + b|/\|w\|_2$, we obtain the geometric relationship:

$$r(d) = \frac{R}{\langle d, u \rangle}, \quad (81)$$

where $\langle d, u \rangle$ is the cosine similarity (alignment) between the search direction and the gradient.

From Eq. (81), it is evident that for a fixed R , $r(d)$ is inversely proportional to the alignment $\langle d, u \rangle$. Thus, $r(d)$ is strictly monotonically decreasing with respect to $\langle d, u \rangle$ for $\langle d, u \rangle > 0$.

Combining this with **Theorem 3**:

- For our method: $\mathbb{E}[\langle d_n, u \rangle] > 0$.
- For random baselines: $\mathbb{E}[\langle d_{\text{rand}}, u \rangle] = 0$ (implying the search direction is orthogonal to the gradient on average, leading to a significantly larger expected boundary distance under the linear approximation).

Therefore, the expected boundary distance for our initialization is strictly smaller in expectation under the local linear model: $\mathbb{E}[r(d_n)] < \mathbb{E}[r(d_{\text{rand}})]$. \square

H Evolution of Intermediate AEs

We analyze the variations in perturbation magnitude r and curvature κ of intermediate AEs as the query increases. The experimental results of 1,000 randomly sampled ImageNet validation images are drawn in Fig. 13. It is easily to find that our method reduce r much faster than ADBA all the time (consistent smaller mean values and standard deviation) on average, making our method find AEs under a given perturbation budget with fewer queries, leading to a higher ASR under the same query limit. As observed in Fig. 13(b), AEs crafted by our DPAttack locate at a higher average curvature region during the query process, leading to much faster reduction in r especially at the early attack stage.

I The Curvature Estimation Method

The curvature at a point on the decision boundary in high-dimensional space quantifies how sharply the boundary bends locally. Due to the computational complexity of calculating the curvature directly, in practice, the curvature can be approximated using the dominant eigenvalue λ_{\max} of the Hessian matrix $H = [\frac{\partial^2 \mathcal{L}(x, y)}{\partial x[i] \partial x[j]}]_{i,j=1}^d$ of the loss function \mathcal{L} with respect to the input x . The estimated curvature κ is obtained via:

$$\kappa \approx \lambda_{\max}(H). \quad (82)$$

In our implementation, we make use of the library PyHessian [61].

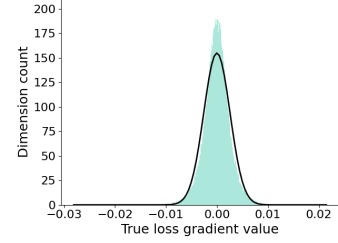


Figure 12: Distribution of the normalized CE loss gradient, $\nabla \mathcal{L}(x, y)/\|\nabla \mathcal{L}(x, y)\|_2$, averaged over 1,000 randomly sampled images from the ImageNet validation set. The distribution closely approximates a Gaussian.

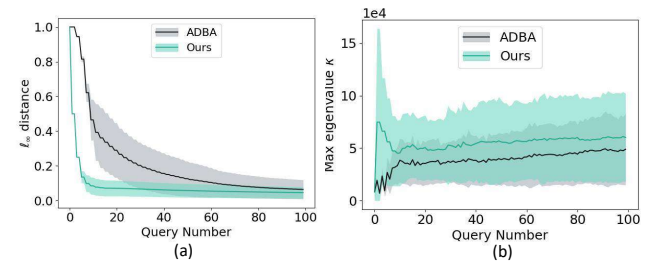


Figure 13: The comparative plot illustrates the variation in (a) the perturbation magnitude r and (b) the curvature κ as the number of queries increases.

J The DBS Algorithm

Since the block size in BDCT plays a critical role in the efficacy of the generated perturbation direction d_n , we propose the Dynamic Blocksize Selection (DBS) algorithm. DBS efficiently identifies the optimal direction that minimizes the initial distance to the decision boundary for each specific image and victim model, providing a superior starting point for subsequent optimization. The key innovation of this algorithm is its parallel evaluation strategy: rather than performing a costly binary search for each candidate to find its exact boundary distance, it assesses all candidates simultaneously at a fixed perturbation magnitude (Lines 6–15 in Algorithm 2). This design drastically reduces the query overhead. To prevent excessive query consumption in edge cases where candidates exhibit nearly identical boundary distances, we stipulate a maximum comparison threshold k_{\max} . If multiple candidates remain indistinguishable after k_{\max} iterations, a final direction is selected via uniform random sampling from the remaining candidate set. The complete procedure is detailed in Algorithm 2.

K The BiLiSearch Algorithm

Conventional methods typically estimate decision boundary distances via independent binary searches for each direction. To achieve a standard precision of 10^{-3} , such approaches require approximately 20 queries per direction [7], which is prohibitively expensive under strict query budgets. We propose BiLiSearch (Algorithm 3) to minimize this overhead through two key strategies: simultaneous evaluation and adaptive search logic.

Algorithm 2 Dynamic Blocksize Selection (DBS) Process

Input: Original image \mathbf{x} , ground-truth label y , victim model \mathcal{F} , candidate block size set \mathbb{W} .

Output: Selected block size w , its direction \mathbf{d}_n^w , and current minimal decision boundary distance r .

```

1: Initialize candidate directions  $D \leftarrow \{\mathbf{d}_n^w \mid w \in \mathbb{W}\}$  where  $\mathbf{d}_n^w$  is the initialization direction for block size  $w$ .
2: Initialize current candidate set  $\mathcal{W}_{curr} \leftarrow \mathbb{W}$ .
3: Initialize binary search bounds  $l \leftarrow 0, h \leftarrow 1$ .
4: Query count  $Q \leftarrow 0$ , iteration  $k \leftarrow 0$ .
5: while  $Q < Q_{max}$  and  $k < k_{max}$  do
6:    $r \leftarrow (l + h)/2$ 
7:   Initialize successful set  $S \leftarrow \emptyset$ .
8:   for each block size  $w \in \mathcal{W}_{curr}$  do
9:     Generate adversarial candidate:  $\mathbf{x}' \leftarrow \text{clip}(\mathbf{x} + r \cdot \mathbf{d}_n^w, [0, 1])$ .
10:    Query victim model:  $y' \leftarrow \mathcal{F}(\mathbf{x}')$ .
11:     $Q \leftarrow Q + 1$ .
12:    if  $y' \neq y$  then
13:       $S \leftarrow S \cup \{w\}$ 
14:    end if
15:   end for
16:   if  $S = \emptyset$  then
17:      $l \leftarrow r$  {All candidates failed, increase magnitude}
18:   else
19:      $h \leftarrow r$  {At least one succeeded, decrease magnitude}
20:      $\mathcal{W}_{curr} \leftarrow S$  {Prune unsuccessful block sizes}
21:   end if
22:    $k \leftarrow k + 1$ 
23: end while
24: Select optimal block size  $w^*$  uniformly at random from  $\mathcal{W}_{curr}$ .
25: return  $w^*, \mathbf{d}_n^{w^*}, h$ .
```

The core of BiliSearch is a simultaneous comparison strategy that refines perturbation distances from coarse to fine granularity. Instead of independent estimations, BiliSearch evaluates two candidate directions at the same magnitude in each iteration. This allows for early termination: if one direction fails to yield an adversarial example at a given distance, the comparison can be pruned immediately without further refinement.

Furthermore, BiLiSearch optimizes the search step based on the current state of the perturbation. Since the optimal distance r is already significantly minimized during the DBS phase, relying solely on aggressive bisection often leads to frequent failures and redundant queries. To address this, we incorporate a line search mechanism that performs conservative, incremental reductions on r . This approach ensures a higher success rate and more efficient query utilization compared to standard bisection. As a result, BiliSearch reduces the average number of queries per comparison from 20 to approximately 13.

L Proof of Theorem 4

L.1 Setup and Notation

Let $\mathbf{u} \in \{\pm 1\}^d$ denote the sign of the true gradient (i.e., $\mathbf{u} = \text{sgn}(\nabla_{\mathbf{x}} \mathcal{L}(\mathbf{x}))$), and let $\mathbf{d} \in \{\pm 1\}^d$ denote the current perturbation direction. For any index subset $S \subseteq [d]$, we define the *signed*

Algorithm 3 BiLiSearch Process

Input: Target classifier \mathcal{F} , clean RGB image \mathbf{x} , initiated directions $\mathbf{d}_n, \mathbf{d}_a$, GT label y , current minimal decision boundary distance r .

Output: Initialization perturbation direction \mathbf{d}_0 and magnitude r_0 .

```

1: Initialization:
2: Query budget  $Q \leftarrow 16$ , line search steps  $t \leftarrow 5$ .
3: Initialize bounds:  $h_1, h_2 \leftarrow r; l_1, l_2 \leftarrow 0$ .
4: Initialize magnitudes:  $r_1 \leftarrow r/2, r_2 \leftarrow r/2$ .
5: Initialize update modes:  $m_1 \leftarrow \text{Bisect}, m_2 \leftarrow \text{Bisect}$ .
6: while  $Q > 0$  do
7:   Generate candidates:
8:    $\mathbf{x}_1 \leftarrow \text{clip}(\mathbf{x} + r_1 \cdot \mathbf{d}_n, [0, 1])$ 
9:    $\mathbf{x}_2 \leftarrow \text{clip}(\mathbf{x} + r_2 \cdot \mathbf{d}_a, [0, 1])$ 
10:  Query model:  $y'_1 \leftarrow \mathcal{F}(\mathbf{x}_1), y'_2 \leftarrow \mathcal{F}(\mathbf{x}_2)$ .
11:  // Update for direction  $\mathbf{d}_n$ 
12:  if  $y'_1 \neq y$  and  $m_1 = \text{Bisect}$  then
13:     $l_1 \leftarrow r_1$ 
14:     $r_1 \leftarrow (h_1 + l_1)/2$  {Bisection update}
15:  else
16:     $m_1 \leftarrow \text{Line}$ 
17:     $r_1 \leftarrow h_1 - (h_1 - l_1)/t$  {Line update}
18:  end if
19:  // Update for direction  $\mathbf{d}_a$ 
20:  if  $y'_2 \neq y$  and  $m_2 = \text{Bisect}$  then
21:     $l_2 \leftarrow r_2$ 
22:     $r_2 \leftarrow (h_2 + l_2)/2$  {Bisection update}
23:  else
24:     $m_2 \leftarrow \text{Line}$ 
25:     $r_2 \leftarrow h_2 - (h_2 - l_2)/t$  {Line update}
26:  end if
27:  if  $(m_1 = \text{Line} \text{ and } y'_1 = y) \text{ or } (m_2 = \text{Line} \text{ and } y'_2 = y)$  then
28:    break
29:  end if
30:   $Q \leftarrow Q - 2$ 
31: end while
32: // Select the direction with smaller perturbation
33: if  $r_1 < r_2$  then
34:   return  $\mathbf{d}_0 \leftarrow \mathbf{d}_n, r_0 \leftarrow r_1$ 
35: else
36:   return  $\mathbf{d}_0 \leftarrow \mathbf{d}_a, r_0 \leftarrow r_2$ 
37: end if
```

correlation $C_{\mathbf{d}}(S)$ and the normalized gain $\Delta(S \mid \mathbf{d})$ as:

$$C_{\mathbf{d}}(S) := \sum_{i \in S} \mathbf{u}_i \mathbf{d}_i, \quad \Delta(S \mid \mathbf{d}) := \frac{|C_{\mathbf{d}}(S)|}{d}. \quad (83)$$

The agreement metric (Hamming similarity) is defined as:

$$A(\mathbf{d}, \mathbf{u}) := \frac{1}{d} \sum_{i=1}^d \mathbb{I}\{\mathbf{d}_i = \mathbf{u}_i\} = \frac{1}{2} \left(1 + \frac{1}{d} \langle \mathbf{d}, \mathbf{u} \rangle \right). \quad (84)$$

Here, \mathbb{I} is the indicator function. Flipping the signs of \mathbf{d} on subset S (i.e. $\mathbf{d}_i \leftarrow -\mathbf{d}_i, i \in S$) increases the agreement by exactly $\Delta(S \mid \mathbf{d})$ if and only if $C_{\mathbf{d}}(S) < 0$. Thus, identifying subsets with large $|C_{\mathbf{d}}(S)|$ is key to rapid optimization. A large magnitude implies high informative value: if positive, the current alignment is preserved; if negative, flipping the signs yields an immediate and significant improvement.

Tree Definitions. Let \mathbf{d}_0 be the initialization direction.

- T_{pat} (Pattern-driven tree): The leaves are the *runs* (maximal constant-sign contiguous segments) of \mathbf{d}_0 . Internal nodes are unions of adjacent runs. Splits occur *only* at run boundaries.
- T_{dyad} (Dyadic tree): A standard binary tree where splits occur at spatial midpoints, independent of \mathbf{d}_0 .

L.2 Assumptions and Lemmas

ASSUMPTION 6 (BLOCK SIGN-COHERENCE OF TRUE GRADIENT). *The true gradient sign \mathbf{u} exhibits a block structure. There exists a partition of $[d]$ into disjoint contiguous blocks $\mathcal{B}^* = \{B_1, \dots, B_K\}$ such that for each B_k , the sign is constant: $\mathbf{u}_i = \sigma_k \in \{\pm 1\}$ for all $i \in B_k$.*

Remark. As evidenced by Fig. 5(a), the true gradient sign \mathbf{u} exhibits distinct block-wise coherence over contiguous neighborhoods. Therefore, we regard this assumption as a data-supported condition rather than a theoretical idealization.

ASSUMPTION 7 (WEAK INFORMATIVE INITIALIZATION). *The initialization \mathbf{d}_0 possesses a weak but strictly positive expected alignment with the true gradient sign \mathbf{u} within spatially coherent regions. Specifically, there exists a bias constant $\delta \in (0, 1/2]$ such that for any run R of \mathbf{d}_0 fully contained within a coherent block of \mathbf{u} (i.e., a valid run), the expected element-wise agreement satisfies:*

$$\mathbb{E} \left[\frac{1}{|R|} \sum_{i \in R} \mathbb{I}\{\mathbf{d}_{0,i} = \mathbf{u}_i\} \right] = \frac{1}{2} + \delta. \quad (85)$$

This condition implies that \mathbf{d}_0 contains a statistically significant signal component, distinguishing it from pure random guessing (where $\delta = 0$).

Remark. This assumption abstracts the requirement for a “warm start” into two distinct properties: (i) **Structural Coherence**: \mathbf{d}_0 must possess finite spatial correlation to form meaningful runs (ensuring the search space is composed of atomic units rather than fragmented noise); and (ii) **Statistical Bias**: The initialization distribution must be positively skewed towards \mathbf{u} . Crucially, Eq. (85) defines an expectation over the random sampling of \mathbf{d}_0 . It does *not* require every individual run in a single realization to be correctly aligned; it suffices that valid runs carry a positive predictive signal *on average*. Our proposed pattern-injected initialization naturally satisfies these conditions: the existence of the positive bias $\delta > 0$ is theoretically supported by Theorem 3 (Frequency Sensitivity Alignment) and empirically evidenced by the positive shift in initial cosine similarity in Fig. 5(b).

We first establish a fundamental property of the signed correlation under partitioning, which will be used to compare the effective gains offered by different tree structures.

LEMMA 5 (GAIN CANCELLATION PRINCIPLE). *For any contiguous set S , let $\{P_j\}$ be any partition of S (i.e., $S = \bigcup_j P_j$, $P_j \cap P_k = \emptyset$). By the Triangle Inequality:*

$$|C_{\mathbf{d}_0}(S)| = \left| \sum_j C_{\mathbf{d}_0}(P_j) \right| \leq \sum_j |C_{\mathbf{d}_0}(P_j)|. \quad (86)$$

The inequality is strict (cancellation occurs) if the signs of $C_{\mathbf{d}_0}(P_j)$ are mixed. Specifically, if S straddles a boundary where the correlation sign changes, the magnitude of the total correlation on S is strictly less than the sum of the magnitudes of its parts.

Table 11: The attack performance on dense prediction tasks. The query limit is 1,000.

Methods	Object Detection			Segmentation		
	ASR	Avg.Q	Med.Q	ASR	Avg.Q	Med.Q
ADBA	39.5	<u>146</u>	73	43.5	364	298
Ours \mathbf{d}_n	70.5	65	<u>27</u>	68.0	227	109
Ours _{opt}	65.0	167	36	63.5	<u>161</u>	36
Ours _{dyn}	69.5	160	26	<u>64.0</u>	160	<u>41</u>

PROOF. Triangle Inequality. \square

Leveraging the gain cancellation principle above, we now compare the quality of candidate nodes made available by the two tree constructions.

LEMMA 6 (AVAILABILITY DOMINANCE). *Let C_{pat} be the set of nodes (runs) available at the leaves of T_{pat} . For any dyadic node $D \in T_{\text{dyad}}$, the gain is no larger than the aggregate gain of its pattern-aligned components. Specifically,*

$$|C_{\mathbf{d}_0}(D)| \leq \sum_{R \in \text{Runs}(D)} |C_{\mathbf{d}_0}(D \cap R)|, \quad (87)$$

where $\text{Runs}(D)$ is the set of runs of \mathbf{d}_0 that intersect D .

PROOF. Let D be an arbitrary node in the dyadic tree. The interval D can be partitioned into disjoint segments based on the runs of \mathbf{d}_0 : $D = \bigcup_j (D \cap R_j)$. The signed correlation on D is the sum of correlations on these segments. By Lemma 5 (taking $P_j = D \cap R_j$):

$$|C_{\mathbf{d}_0}(D)| \leq \sum_j |C_{\mathbf{d}_0}(D \cap R_j)|.$$

In T_{pat} , the leaves are the full runs R_j . The algorithm selects nodes based on normalized gain $\Delta(S \mid \mathbf{d})$. If D straddles a boundary between runs of opposite signs (which happens frequently in T_{dyad} because it ignores \mathbf{d}_0 's structure), terms in the sum cancel out, strictly reducing the gain $|C_{\mathbf{d}_0}(D)|$. In contrast, the nodes R_j in T_{pat} are defined by the constant-sign regions of \mathbf{d}_0 . By construction, they suffer zero cancellation from initialization sign changes. While a run R_j may still span a boundary of the true gradient \mathbf{u} , it is structurally superior to D , as the latter is susceptible to gain cancellation arising from *both* \mathbf{d}_0 and \mathbf{u} . Thus, the search space of T_{pat} offers candidates with higher non-cancelled gain potential than arbitrary dyadic intervals. \square

L.3 Proof of Theorem 4

With the above assumptions ensuring block-level signal coherence (Assumptions 6–7) and Lemmas 5–6 characterizing the structural advantage of the pattern-driven candidate pool, we now establish the per-query alignment dominance.

THEOREM 4 (PER-QUERY SIGN ALIGNMENT DOMINANCE). Let $\mathbf{u} = \text{sgn}(\nabla_{\mathbf{x}} \mathcal{L})$ be the true gradient sign, and let $\mathbf{d}_t \in \{\pm 1\}^d$ be the perturbation direction after t queries. We measure sign alignment using the agreement $A(\mathbf{d}_t, \mathbf{u}) := \frac{1}{d} \sum_{i=1}^d \mathbb{I}\{\mathbf{d}_{t,i} = \mathbf{u}_i\}$. Under the assumptions of local block coherence (Asmp. 6) and a weakly positive initial correlation (Asmp. 7), the expected agreement A_t after t queries satisfies:

$$\mathbb{E}[A_t^{\text{pat}}] \geq \mathbb{E}[A_t^{\text{dyad}}], \quad \forall t \in \mathbb{N}, \quad (88)$$

where pat and dyad denote the pattern-driven strategy and the blind dyadic baseline, respectively.

PROOF. The proof relies on the greedy nature of the selection policy and the superior quality of the candidate pool available in the pattern tree.

- (1) **Decomposition:** The agreement at step t is the cumulative sum of gains: $A_t = A_0 + \sum_{j=1}^t G_j$, where G_j is the agreement improvement at the j -th query. Since A_0 is identical for both, it suffices to show $\mathbb{E}[G_j^{\text{pat}}] \geq \mathbb{E}[G_j^{\text{dyad}}]$.
- (2) **Candidate Selection Policy:** Both methods use the same greedy rule. They simply look at all currently available nodes and pick the one that offers the largest possible gain $\Delta(S \mid \mathbf{d})$. In practice, this is approximated by selecting the candidate that yields the maximum reduction in the distance to the decision boundary. Therefore, the improvement at step j is determined by the best candidate found in the tree at that moment.
- (3) **Structural Advantage:** Consider the composition of the candidate nodes.
 - **Pattern Tree:** The candidates are the *runs* of \mathbf{d}_0 . By definition, a run is a maximal segment of constant sign. Thus, pattern nodes are “atomic” with respect to \mathbf{d}_0 and suffer *zero internal cancellation* from initialization sign changes.
 - **Dyadic Tree:** The candidates are arbitrary spatial intervals. By Lemma 6, a dyadic node D is structurally the summation of the pattern runs it covers. If D covers runs of opposing signs (e.g., a positive region adjacent to a negative region), these components mathematically cancel each other out, strictly reducing the magnitude of the total correlation: $|C(D)| < \sum |C(R_i)|$.
- (4) **Availability of High-Gain Candidates (Max-Pooling Argument):** This difference in candidate exposure can be interpreted as a max-pooling effect induced by the absence of gain cancellation (Lemma 5). Since the algorithm is greedy, it always selects the candidate with the largest instantaneous gain from the current pool. A key distinction between the two trees lies in how local signals are pooled. In T_{dyad} , dyadic nodes often mix adjacent regions with opposing signs. For a mixed node composed of two runs with gains a and b , the effective gain available to the dyadic strategy is proportional to $|a + b|$, which can be severely reduced by cancellation.

Table 12: The attack performance on ImageNet (adversarial trained WideResNet-50) under different perturbations.

Metrics $\epsilon (\ell_\infty)$	ASR			Avg.Q			Med.Q		
	ADBA	Ours _{opt}	Ours _{dyn}	ADBA	Ours _{opt}	Ours _{dyn}	ADBA	Ours _{opt}	Ours _{dyn}
0.03	26.0	28.0	27.0	158	153	162	56	92	110
0.05	45.0	50.5	48.5	143	143	191	58	73	90
0.08	73.0	73.5	73.0	96	116	121	41	40	48
0.10	85.5	87.0	86.5	74	89	82	35	26	33

In contrast, T_{pat} decomposes the search space along sign-consistent runs. The same mixed region is exposed as separate atomic candidates with gains $|a|$ and $|b|$, allowing the greedy rule to select $\max(|a|, |b|)$.

By the triangle inequality,

$$\max(|a|, |b|) \geq \frac{1}{2}|a + b|,$$

and in the presence of sign cancellation, $\max(|a|, |b|)$ can be substantially larger than $|a + b|$. Therefore, for every dyadic candidate, T_{pat} provides a candidate with no smaller (and often strictly larger) available gain. As a result, the maximum gain attainable at each greedy step under T_{pat} is, in expectation, no worse (and often strictly better) than that under T_{dyad} .

- (5) **Probabilistic Dominance of Boundaries:** Beyond structural considerations, Assumption 7 ensures that the pattern boundaries are statistically informative about the true gradient structure. Finally, we address the alignment with the true gradient \mathbf{u} . While it is theoretically possible for a blind dyadic cut to fortuitously align with a boundary of \mathbf{u} (a “lucky guess”), the Dyadic strategy is statistically disadvantaged.
- **Dyadic (Blind):** The splits are fixed (e.g., at $d/2$) and independent of the signal structure. The probability that a fixed dyadic partition aligns well with the unknown block boundaries of \mathbf{u} is small in general, especially when block boundaries are not synchronized with the grid.
- **Pattern (Correlated):** The splits follow the boundaries of \mathbf{d}_0 . Under Assumption 7, \mathbf{d}_0 is spatially correlated with \mathbf{u} . This implies that the boundaries of \mathbf{d}_0 act as noisy but informative predictors of the boundaries of \mathbf{u} . Therefore, a pattern-defined node is significantly more likely to be *sign-coherent* with respect to \mathbf{u} (preserving full gain) than an arbitrary dyadic interval. Combined with the Max-Pool argument, this ensures:

$$\mathbb{E}[G_j^{\text{pat}}] \geq \mathbb{E}[G_j^{\text{dyad}}].$$

- (6) **Conclusion:** Summing the expected gains over t steps yields the theorem statement. □

M Proof of Theorem 5

THEOREM 5 (QUERY COMPLEXITY UNDER BLOCK SIGN-COHERENCE). *Under Assumptions 6 and 7, let the true gradient sign \mathbf{u} consist of K spatially coherent blocks $\{B_k\}_{k=1}^K$. To identify descent directions aligned with \mathbf{u} , the expected query complexities for dyadic search (T_{dyad}) and pattern-driven search (T_{pat}) satisfy:*

$$T_{\text{dyad}} = \Omega \left(\sum_{k=1}^K \log_2 \frac{d}{|B_k|} \right), \quad T_{\text{pat}} = O \left(\sum_{k=1}^K \gamma_k \right), \quad (89)$$

where γ_k is the number of \mathbf{d}_0 -runs intersecting block B_k . In particular, the pattern-driven strategy is asymptotically more efficient in expectation when $\gamma_k < \log_2(d/|B_k|)$ on average.

PROOF. The proof compares how efficiently the two strategies expose non-cancelled descent gain under block sign-coherence.

Setup. We refer to the signed correlation $C_d(S)$ over a subset S as its signed descent gain. Under Assumption 7, for any run $R \subseteq B_k$ fully contained in a true block, the expected gain contribution is strictly positive.

Dyadic Strategy. The dyadic strategy recursively partitions coordinates by index. If a true block B_k is fragmented into multiple dyadic cells at a given depth, cells are likely to contain mixed signs of \mathbf{u} , which leads to partial cancellation of signed gain. In expectation, the magnitude of the gain is significantly reduced compared to a fully contained block. In the worst case, or in expectation over random block alignments, isolating a region fully contained in B_k requires the tree to reach depth $\Omega(\log_2(d/|B_k|))$, yielding

$$T_{\text{dyad}} = \Omega \left(\sum_{k=1}^K \log_2(d/|B_k|) \right).$$

Pattern-Driven Strategy. The pattern-driven strategy partitions coordinates along sign-consistent runs of the initial direction \mathbf{d}_0 . For any run R such that $R \cap B_k \neq \emptyset$, there exists a contiguous sub-run $R' \subseteq R \cap B_k$ that is fully contained in the true block B_k . By Assumption 7, such sub-runs admit strictly positive expected signed descent gain.

Importantly, the pattern-driven strategy explicitly enumerates runs that intersect with B_k , and the number of such candidates is denoted by γ_k . Each candidate can be evaluated with $O(1)$ queries, and the existence of a fully contained sub-run ensures that informative descent directions are exposed without requiring further partitioning. Therefore,

$$T_{\text{pat}} = O \left(\sum_{k=1}^K \gamma_k \right).$$

Conclusion. The comparison highlights the efficiency of structural priors. While the dyadic strategy requires deep partitioning proportional to the log-inverse of the block density ($\log(d/|B_k|)$) to resolve the signal, the pattern-driven strategy exploits the existing coarse alignment, requiring only $O(\gamma_k)$ queries per block. Since γ_k is a small constant (representing the number of initialization segments touching the block) and $\log(d/|B_k|)$ grows as the true

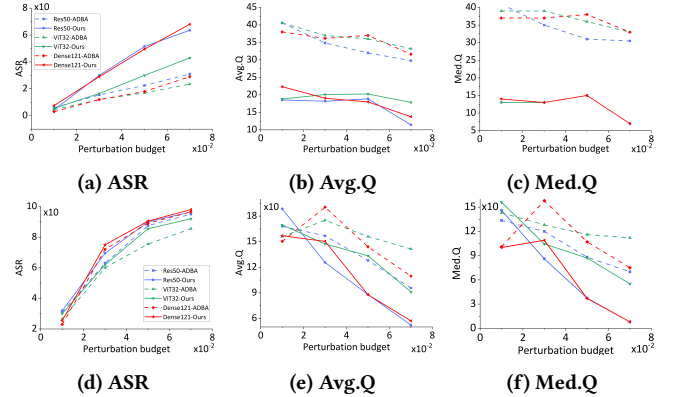


Figure 14: The attack performance comparison on the ImageNet test dataset under different perturbation budgets. We set two different query budgets to represent low and high query budget scenarios: 50 ((a)–(c)) and 500 ((d)–(e)).

gradient becomes higher-frequency, the pattern-driven strategy is strictly superior. \square

Remark (Run Width vs. Block Granularity). Empirically, we observe that the number of sign-consistent runs induced by the initial direction \mathbf{d}_0 is significantly smaller than the number of true gradient blocks across ImageNet images. For example, over more than 50,000 ground-truth gradient blocks, the number of runs is approximately 20k, 11k, and 6k for block sizes $w = \{4, 8, 16\}$, respectively. This implies that individual runs typically span multiple gradient blocks and, consequently, that the intersection between a run and a block often contains a non-trivial contiguous sub-run fully contained within the block.

N Detailed Experimental Settings

Victim Models. For CIFAR-10, we select standard ResNet-18 and VGG-16-BN models [45], alongside an adversarially trained WideResNet [13]. For ImageNet-1K, we target a diverse array of high-performing architectures from the Torchvision library [45], including ResNet-50, ViT-B-32, DenseNet-121, EfficientNet-B3, ConvNeXt-Base, Inception-v3, SwinV2-T, DeiT-B, and RegNet-X-8GF. Additionally, we evaluate an adversarially trained WideResNet-50 (trained with $\ell_\infty = 8/255$ [19]). Regarding foundation models [46], we employ the ViT-H-14-CLIP-A-336 [29], chosen for its superior zero-shot performance on ObjectNet. For downstream tasks, we evaluate FasterRCNN-ResNet50-FPN-V2 [45] (object detection) and SAM-ViT-B [33] (segmentation). Finally, we adopt the top-performance NoisyMix [20] and HMany [26] models from RobustBench library [13] for ImageNet-C, and a standard MLP from the MedMNIST library [58, 60] for PathMNIST.

Implementation Details. In DPAttack, for low-frequency filtering, the decomposition level is set to its maximum feasible depth, $dl = \lfloor \log_2(\bar{w}) \rfloor$. Empirical analysis shows that while results are marginally sensitive to dl within its valid range, larger values generally yield superior performance. For baselines requiring Monte Carlo gradient estimation (HSJA, Bounce, and Tangent), we tune their batch sizes via grid search to ensure fairness in low-query

Table 13: The attack performance on CIFAR-10 (VGG-16-BN) under $\ell_\infty = 0.05$ constraint.

Metrics	ASR										Avg.Q										Med.Q									
	MaxQ	HSJA	BouR	BouT	TtBA	HRayS	ADBA	Ours _{opt}	Ours _{dyn}	HSJA	BouR	BouT	TtBA	HRayS	ADBA	Ours _{opt}	Ours _{dyn}	HSJA	BouR	BouT	TtBA	HRayS	ADBA	Ours _{opt}	Ours _{dyn}					
5	0.0	0.0	0.5	0.0	1.5	0.0	4.0	0.0	-	-	5	-	5	-	5	-	-	-	5	-	5	-	5	-	5	-	-	-	-	
10	0.0	0.0	2.5	0.0	1.5	0.0	14.5	2.5	-	-	7	-	10	-	6	9	-	-	7	-	10	-	6	6	-	-	-	-	-	
20	2.5	2.5	2.5	0.0	3.5	2.0	14.5	18.5	14	14	7	-	19	17	6	14	14	14	7	-	20	17	6	14	-	-	-	-	-	
50	24.5	24.5	14.0	0.0	8.0	13.0	30.0	30.0	44	44	33	-	39	35	25	24	48	48	40	-	47	37	24	18	-	-	-	-	-	
80	32.0	33.0	25.0	4.0	11.0	24.5	45.5	41.0	45	47	49	71	49	47	39	35	49	50	41	71	49	49	37	29	-	-	-	-	-	
100	32.5	37.5	22.5	5.5	18.0	31.5	49.5	50.5	45	47	44	73	69	57	43	45	49	50	41	68	55	40	39	-	-	-	-	-		
150	41.5	40.5	16.0	8.5	26.5	51.0	62.0	64.0	82	81	64	91	93	83	61	61	89	89	79	72	98	85	52	56	-	-	-	-	-	
200	44.0	41.5	27.0	9.0	37.0	66.0	76.0	73.0	81	84	115	106	121	104	81	74	89	89	82	107	122	104	66	65	-	-	-	-	-	
250	45.0	45.0	27.0	15.5	45.5	75.0	80.0	80.5	92	85	99	147	143	118	88	88	89	90	80	141	150	117	69	74	-	-	-	-	-	
300	45.5	45.0	28.0	21.0	57.0	79.0	82.5	85.5	89	85	106	185	173	125	94	99	90	90	80	214	179	120	72	82	-	-	-	-	-	
400	42.0	42.0	29.0	32.5	71.5	86.0	87.5	90.5	87	84	120	259	212	144	109	112	89	89	82	298	209	127	79	87	-	-	-	-	-	
500	44.0	43.0	29.5	40.0	76.5	91.0	92.5	91.5	83	86	115	293	227	161	127	116	89	90	81	299	217	132	83	87	-	-	-	-	-	
1k	47.0	49.5	35.0	64.0	91.0	98.0	98.5	98.5	137	133	239	491	305	205	163	161	140	139	133	487	265	147	96	92	-	-	-	-	-	
2k	48.5	48.0	37.0	81.5	98.0	99.5	100.0	99.0	201	130	320	657	387	220	178	166	140	139	132	591	288	147	107	94	-	-	-	-	-	
3k	52.0	47.5	40.0	92.5	99.5	100.0	100.0	100.0	180	136	346	873	393	229	171	188	139	139	134	698	290	147	104	98	-	-	-	-	-	

Table 14: The attack performance on CIFAR-10 (ResNet-18) under $\ell_\infty = 0.05$ constraint.

Metrics	ASR										Avg.Q										Med.Q									
	MaxQ	HSJA	BouR	BouT	TtBA	HRayS	ADBA	Ours _{opt}	Ours _{dyn}	HSJA	BouR	BouT	TtBA	HRayS	ADBA	Ours _{opt}	Ours _{dyn}	HSJA	BouR	BouT	TtBA	HRayS	ADBA	Ours _{opt}	Ours _{dyn}					
5	0.0	0.0	0.0	0.0	0.5	0.0	4.5	0.0	-	-	-	-	5	-	5	-	-	-	-	-	-	5	-	5	-	-	-	-	-	-
10	0.0	0.0	0.0	0.0	0.5	0.0	16.5	2.0	-	-	6	-	10	-	6	8	-	-	-	-	10	-	6	8	-	-	-	-	-	-
20	4.5	4.5	1.5	0.0	1.0	0.0	17.0	18.5	13	13	7	-	19	-	7	14	13	13	5	-	19	-	6	14	-	-	-	-	-	
50	27.0	27.0	17.5	0.0	5.0	10.0	36.0	31.0	41	41	37	-	44	38	25	24	48	48	40	-	48	39	23	18	-	-	-	-	-	
80	34.0	31.5	23.5	14.5	11.5	22.5	45.0	48.0	47	46	47	71	59	53	33	37	50	49	41	70	62	53	29	30	-	-	-	-	-	
100	37.0	38.0	27.5	13.5	13.5	32.5	49.5	51.0	48	48	51	70	74	64	38	40	49	49	41	69	79	66	31	35	-	-	-	-	-	
150	43.5	45.5	19.5	19.5	22.5	56.0	61.5	61.5	81	82	76	93	97	88	56	55	89	89	80	72	110	88	41	50	-	-	-	-	-	
200	41.0	46.0	26.0	19.5	33.0	64.5	70.0	72.5	84	83	101	95	127	100	70	73	89	90	80	72	122	100	48	56	-	-	-	-	-	
250	42.5	48.0	26.5	31.5	44.5	74.5	79.5	78.5	91	86	100	134	157	116	89	84	89	89	80	137	147	107	60	61	-	-	-	-	-	
300	44.0	47.5	29.5	35.5	53.5	78.5	85.5	83.0	86	90	119	153	179	126	102	95	89	89	81	139	191	113	72	63	-	-	-	-	-	
400	45.5	41.5	32.5	47.0	63.5	87.0	89.0	88.5	89	87	110	209	207	146	111	109	89	89	81	214	207	116	77	69	-	-	-	-	-	
500	46.5	47.0	30.0	57.0	75.0	93.0	94.0	92.0	94	90	141	247	246	166	124	122	89	89	84	218	235	123	84	74	-	-	-	-	-	
1k	49.5	53.0	36.0	77.5	93.5	97.0	98.0	97.0	147	145	222	379	332	191	152	150	138	139	131	302	279	128	95	83	-	-	-	-	-	
4k	53.5	53.0	41.5	96.0	99.5	100.0	100.0	100.0	393	140	340	975	411	214	183	192	140	139	134	774	289	130	106	97	-	-	-	-	-	

Table 15: The attack performance on ImageNet (ViT-B-32) under $\ell_\infty = 0.05$ constraint.

Metrics	ASR										Avg.Q										Med.Q									
	MaxQ	HSJA	BouR	BouT	TtBA	HRayS	ADBA	Ours _{opt}	Ours _{dyn}	HSJA	BouR	BouT	TtBA	HRayS	ADBA	Ours _{opt}	Ours _{dyn}	HSJA	BouR	BouT	TtBA	HRayS	ADBA	Ours _{opt}	Ours _{dyn}					
5	0.0	0.0	3.5	0.0	0.5	0.0	20.0	-	-	-	5	-	5	-	5	-	-	-	-	5	-	5	-	5	-	-	-	-	-	
10	0.0	0.0	9.0	0.0	0.5	0.0	18.5	-	-	-	6	-	10	-	6	-	-	-	-	6	-	10	-	6	-	-	-	-	-	
20	2.0	2.0	9.0	0.0	0.5	2.0	19.0	17.0	14	14	6	-	20	18	12	18	14	14	6	-	20	18	10	19	-	-	-	-	-	
50	2.5	2.5	12.5	0.0	10.5	17.0	30.0	30.0	14	14	8	-	42	36	20	25	14	14	6	-	40	36	15	20	-	-	-	-	-	
80	9.5	9.5	13.0	6.5	17.5	30.0	41.5	43.5	48	48	9	75	57	49	32	38	60	60	6	75	57	48	26	27	-	-	-	-	-	
100	10.0	8.0	15.5	9.0	22.0	35.5	44.5	48.0	45	45	25	80	66	55	36	45	60	60	6	80	72	52	29	35	-	-	-	-	-	
200	11.0	12.0	15.5	15.0	36.5	52.5	64.5	65.0	77	82	46	115	103	86	71	71	100	100	6	120	98	74	54	55	-	-	-	-	-	
300	14.0	11.5	13.0	19.5	44.0	63.5	74.5	75.5	85	81	35	143	129	113	97	96	100	99	6	146	117	88	65	71	-	-	-	-	-	
400</td																														

regimes. This adjustment is necessary because their default batch size (100) leads to 0% ASR whenever the query budget $Q_{\max} < 100$. **Dense Prediction Tasks.** For the results in Tables 8 and 11, we define task-specific success criteria: (i) Object Detection: an attack succeeds if the per-image Average Precision (AP) drops below 0.2; (ii) Segmentation: success is defined as reducing the prediction IoU to < 0.5 . Strictly adhering to the hard-label setting, our algorithm only accesses predicted bounding boxes or masks during the attack process. Confidence scores are solely utilized for final AP calculation during the evaluation phase and are never used to guide the attack generation.

O Additional Results under ℓ_∞ Constraints

O.1 Performance under Different Perturbation Budgets

Fig. 14 illustrates the attack performance of DPAttack versus ADBA under varying ℓ_∞ constraints. In the low-query regime (Figs. 14a–c): our method maintains a clear ASR advantage that scales with the perturbation magnitude, while requiring significantly fewer queries to find successful adversarial examples. In the high-query regime (Figs. 14d–f): DPAttack remains superior across different perturbation levels. The only marginal exception occurs at an extremely small bound of $\ell_\infty = 0.01$, where our method shows a slightly higher average query count. This is primarily because DPAttack successfully converts “hard samples” that ADBA fails to attack; these more challenging cases naturally demand higher query counts, which increases the overall average but results in a superior final ASR.

O.2 Generalization across Architectures and Domains

To complement the results in Sec. 5.2, we provide extensive evaluations across diverse architectures and datasets. Tables 13–16 report the performance on VGG-16-BN and ResNet-18 (CIFAR-10), as well as ViT-B-32 and DenseNet-121 (ImageNet) across multiple query budgets. Table 17 further extends these evaluations to a wider range of SOTA ImageNet architectures.

Beyond standard natural images, we evaluate DPAttack on corrupted (ImageNet-C) and biomedical (PathMNIST) domains (see Table ??). Our method consistently outperforms SOTA hard-label attacks in both ASR and query efficiency across all tested models, confirming the generalization of our proposed method.

O.3 Robustness against Adversarial Training

Table 12 presents comparative results against an adversarially trained WideResNet-50. Our method achieves a consistently higher ASR than the second-best baseline, ADBA, across various perturbation levels while maintaining competitive query efficiency. Notably, the ASR gains—though numerically modest—represent a significant improvement in the challenging context of attacking robust models.

O.4 Generalization on Dense Prediction Tasks

Beyond the results in Table 8 of the main manuscript, which demonstrate the superiority of our method under a strict query budget (50), Table 11 further shows that our approach maintains a performance margin of over 30% even when the query limit is relaxed to 1,000.

P Additional Results Under ℓ_2 Constraint

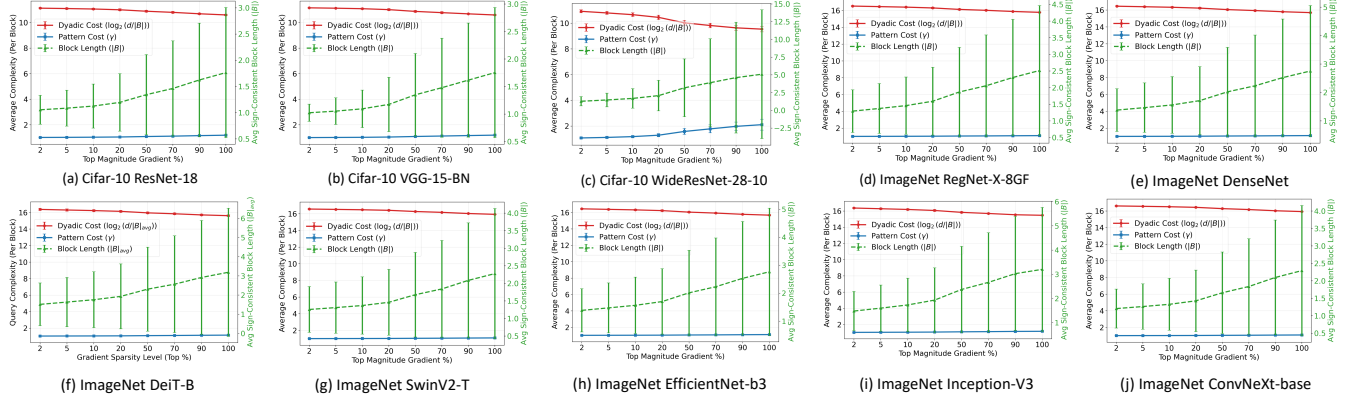
While DPAttack is primarily tailored for the structural characteristics of ℓ_∞ perturbations, we evaluate its performance under ℓ_2 constraints to demonstrate its versatility. Table 18 compares DPAttack against SOTA methods specifically optimized for the ℓ_2 metric, such as SurFree and Tangent. Despite its ℓ_∞ -focused design, DPAttack achieves superior ASR and query efficiency—particularly in low-query regimes—validating its robust generalization across different distance metrics.

Table 17: The attack performance on ImageNet across diverse architectures under $\ell_\infty = 0.05$ constraint.

Models	EfficientNet-b3			ConvNeXt-base			Inception-v3			SwinV2-T			DeiT-B			RegNet-X-8GF		
MaxQ	ADBA	Ours _{opt}	Ours _{dyn}	ADBA	Ours _{opt}	Ours _{dyn}	ADBA	Ours _{opt}	Ours _{dyn}	ADBA	Ours _{opt}	Ours _{dyn}	ADBA	Ours _{opt}	Ours _{dyn}	ADBA	Ours _{opt}	Ours _{dyn}
50	24.5	36.5	44.5	4.5	17.0	18.5	14.5	44.0	48.5	10.5	16.5	18.5	5.5	8.0	18.5	20.5	35.5	65.0
500	85.5	87.0	85.0	72.5	75.5	68.0	85.0	85.5	87.0	52.0	67.5	67.5	46.5	55.0	62.0	88.0	92.0	91.0

Table 18: The attack performance comparison on ImageNet test dataset under $\ell_2 = 5$ constraint.

Victims	Metrics	ASR							Avg.Q							Med.Q						
		HSJA	BouR	BouT	SurFree	Tangent	Ours _{opt}	Ours _{dyn}	HSJA	BouR	BouT	SurFree	Tangent	Ours _{opt}	Ours _{dyn}	HSJA	BouR	BouT	SurFree	Tangent	Ours _{opt}	Ours _{dyn}
ResNet-50	100	5.5	5.5	5.5	8.5	8.0	14.5	33.0	39	31	40	43	62	39	70	50	19	37	37	44	36	100
	500	8.0	6.5	6.5	18.0	18.0	34.5	46.0	104	80	133	168	199	171	252	89	79	76	110	150	125	228
	1k	9.5	7.5	8.0	26.0	25.0	44.5	54.5	162	124	163	351	415	295	419	140	136	126	280	310	202	333
	5k	10.0	9.0	9.0	52.0	61.5	67.5	69.0	884	525	423	1,410	1,590	1,088	1,135	141	138	128	1,062	1,304	572	487
Dense-121	100	5.0	5.0	4.0	7.5	7.0	15.5	37.5	42	49	19	46	59	32	73	50	47	9	39	45	24	100
	500	8.0	6.0	6.5	18.0	13.0	25.0	41.5	113	139	129	306	490	132	261	90	88	78	119	150	59	282
	1k	5.5	6.5	8.0	22.5	22.0	33.5	42.5	131	113	249	306	490	264	390	140	137	131	229	485	143	282
	5k	9.5	8.5	7.0	53.0	66.0	67.5	69.5	568	509	367	1,727	1,889	1,323	1,493	142	138	128	1,334	1,541	1,052	1,006
ViT-B-32	100	3.5	6.0	5	5.5	6.5	15.5	43.0	21	43	59	53	64	42	79	18	51	39	48	70	40	100
	500	10.0	13.5	11.0	13.5	16.5	30.5	51.5	157	236	158	171	265	138	279	91	182	79	106	219	99	275
	1k	11.5	20.5	20.5	19.5	22.0	36.5	56.5	263	486	504	335	493	231	475	141	500	490	287	482	138	331
	5k	29.5	54.0	57.5	47.0	55.5	59.5	71.0	1,768	1,907	1,985	1,847	1,708	1,039	1,593	1,296	1,832	1,823	1,422	1,199	439	637

**Figure 15: Extensive validation of Theorem 5 on diverse datasets and architectures. The results consistently confirm that salient gradients exhibit rapid sign oscillations ($|B| \approx 1$), validating the universality of the query complexity gap derived in Theorem 5.**

